ALIN Framework (Adaptive Lethal Intersection Network): Pan-Cancer Generalization of Tri-Axial Combination Therapy to Prevent Drug Resistance

Roy Erzurumluoğlu*†

Maastricht University, Bachelor of Natural Sciences, Maastricht, The Netherlands. Current affiliation: none.

February 8, 2026

Abstract

Cancer drug resistance arises when tumors shift signaling through compensatory pathways upon targeted inhibition. Liaki et al. [1] (PNAS 2025) demonstrated a solution in pancreatic cancer: simultaneously targeting three independent signaling axes, downstream, upstream, and orthogonal, prevents resistance because tumor cells survive through *any one* remaining active node.

We present ALIN Framework (Adaptive Lethal Intersection Network), a computational pipeline that applies this tri-axial inhibition principle computationally across DepMap cancer types. ALIN identifies cancer-specific viability paths, discovers which target combinations intersect every path via minimal hitting set optimization, and generates **ranked triple combinations** scored for tri-axial coverage, synergy, resistance prevention, toxicity, and druggability.

Across 96 cancer types, we generate predictions for **77 cancers** with **37.2% any-overlap recall** ($|G \cap T| \geq 1$) and **16.3% pair-overlap recall** ($|G \cap T| \geq 2$) against 43 independently curated multi-target gold-standard combinations spanning 25 cancer types (60.0% any-overlap and 28.0% pair-overlap on the 25 testable entries where cancer type and target modality are compatible with DepMap CRISPR data; 3.2× the 11.6% global-frequency baseline; $p < 0.001$ vs. random, binomial test). Cancer-level precision—the fraction of evaluable cancer types whose predicted triple contains ≥ 1 gold-standard target—is **47.1%** (8/17 evaluable cancers; 58.3% on the 12 testable cancers), exceeding the global-frequency baseline (17.6%) and random (32.9%). A hub-gene penalty in the triple-scoring stage corrects STAT3's algorithmic over-representation, producing clinically plausible, cancer-specific predictions. Key findings: (1) **STAT3** appears in 78% of MHS predictions (60/77 cancers), consistent with its known constitutive activation [2, 3] and its mathematical favorability as a high-degree hub in hitting-set optimization; however, a proportional hub penalty in ranked triple scoring reduces STAT3 dominance, yielding predictions enriched for validated oncogene targets (EGFR, BRAF, KRAS, MET); (2) a convergent tri-axial architecture emerges in MHS: STAT3 (orthogonal) + cell cycle regulators (downstream) + cancer-specific driver (upstream); (3) an ODE-based pathway shifting simulation, parameterized to encode the tri-axial hypothesis (not fit to experimental data; see Limitations), illustrates that under these assumptions tri-axial combinations yield ~30% lower tumor viability than same-axis combinations across five cancers; (4) 88% of MHS predictions include at least one druggable target, and 100% of ranked triples are fully druggable. ALIN's any-overlap recall (37.2%) exceeds

---

*Corresponding author: roy.erzurumluoglu@gmail.com
†ORCID: 0009-0000-9523-881X

global-frequency (11.6%) and global random (21.9%) baselines but remains below a curated driver-gene baseline (44.2%), indicating room for improvement through subtype-specific analysis and expression data integration. A candidate-pool random baseline sampling from the same per-cancer gene pool the pipeline uses achieves only 0.2% any-overlap, confirming that the scoring stages—not merely DepMap pre-filtering—drive performance. Cancer-level precision (47.1%) further confirms that nearly half of ALIN's evaluable predictions recover at least one validated target. When restricted to the 25 testable entries, ALIN achieves 60.0% any-overlap recall, equalling the driver-gene baseline (60.0%) and far exceeding both global-frequency (12.0%) and global random (33.1%) baselines.

Keywords: cancer — drug resistance — tri-axial inhibition — combination therapy — DepMap — STAT3 — pathway shifting — precision oncology

Corresponding author: roy.erzurumluoglu@gmail.com

Introduction

Single-agent cancer therapies fail because tumors adapt: when one signaling pathway is inhibited, parallel or compensatory pathways sustain tumor cell survival. This *pathway shifting* is the fundamental mechanism of acquired drug resistance [6, 7]. Combination therapy addresses this by simultaneously blocking multiple survival axes, but the vast combinatorial space ($\sim$20,000 genes $\rightarrow$ millions of possible combinations) makes rational design essential.

Liaki et al. [1] recently demonstrated a powerful solution to drug resistance in pancreatic ductal adenocarcinoma (PDAC). They showed that PDAC tumor cells maintain viability through three independent signaling nodes: **downstream** (RAF1), **upstream** (EGFR), and **orthogonal** (STAT3) to KRAS signaling. Crucially, expression of *any single* node is sufficient to maintain tumor cell proliferation, ablating two nodes triggers compensatory activation of the third (e.g., RAF1+EGFR ablation activates STAT3 via FYN kinase phosphorylation [8, 9]). Only simultaneous targeting of all three axes, pharmacologically achieved with daraxonrasib (RAS inhibitor) [10], afatinib (EGFR/HER2 inhibitor) [11, 12], and SD-36 (STAT3 PROTAC) [13], induced complete tumor regression with no resistance for >200 days. Dual combinations failed in all tested permutations [1].

This tri-axial inhibition principle provides a biologically principled framework for combination therapy design: to prevent pathway shifting, one must simultaneously block the downstream effector, the upstream activator, and the orthogonal survival node. However, generalizing this principle beyond PDAC requires answering a cancer-specific question: *which genes occupy the downstream, upstream, and orthogonal positions for each cancer type?*

We present ALIN Framework (Adaptive Lethal Intersection Network), a computational pipeline that addresses this question systematically. ALIN infers cancer-specific viability paths (functional survival mechanisms from DepMap + OmniPath data), then identifies target combinations that cover every viability axis. The **minimal hitting set (MHS)** [14, 15] formalizes target selection as a combinatorial optimization problem, while **ranked triple combinations** scored for pathway diversity (tri-axial coverage), synergy, resistance prevention, and toxicity provide computationally prioritised predictions requiring extensive preclinical validation.

Our contributions: (1) computational extension of the tri-axial principle to 77 cancer types (noting that extension from one experimentally validated system to 76 untested cancers is a hypothesis, not a demonstration); (2) computational prediction of convergent target architecture across cancers, with a hub-gene penalty that corrects STAT3's algorithmic over-representation in ranked triples (see Limitations); (3) ranked triple combinations with multi-source validation; (4) honest benchmarking against 43 independently curated multi-target gold-standard combinations

2

(37.2% any-overlap recall, 16.3% pair-overlap recall, 47.1% cancer-level precision, 3.2× global-frequency baseline; 60.0%, 28.0%, and 58.3% on the 25 testable entries), with LOCO partitioned evaluation, four baselines including a driver-gene comparator and a candidate-pool random baseline (0.2% any-overlap, confirming that scoring—not pre-filtering—drives performance) [16, 17], and a KNOWN_SYNERGIES ablation confirming zero circularity (identical predictions with curated synergy pairs disabled); (5) ODE-based simulation illustrating, as a deductive consequence of explicitly assumed compensatory signaling parameters (not an independent prediction), an ∼30% viability advantage of tri-axial over same-axis combinations.

Methods

Data sources

We use DepMap [18, 19] release 24Q4 (accessed January 2026) for gene dependency $D_{g,\ell}$ (Chronos score [18] from CRISPRGeneEffect.csv), cell line metadata (Model.csv), and cancer type mapping via OncoTree (OncotreePrimaryDisease). OmniPath [20] provides the directed signaling network $G = (V, E)$ (accessed January 2026; cached for reproducibility). PRISM [21] and GDSC [22, 23] supply drug sensitivity data for validation. All data versions and access dates are documented in VERSION_INFO.md (Supplementary Methods, Section S1).

Viability path inference

Viability paths represent independent survival mechanisms that must each be blocked to prevent pathway shifting and resistance [1]. The Liaki et al. [1] finding that PDAC cells survive through *any one* of three signaling axes (RAF1, EGFR, STAT3) motivates our approach: we infer multiple distinct viability paths per cancer, then seek combinations that cover all of them. We infer paths by four complementary approaches: co-essentiality clustering, signaling topology, cancer-specific statistical testing, and perturbation-response signatures.

1. Essentiality and selectivity. A gene is considered essential if its DepMap Chronos score is below -0.5 and *selective* if it is essential in $\geq 30\%$ of cell lines for that cancer type. These cutoffs mirror common practice in DepMap-derived analyses [18, 24, 25]. A systematic threshold sensitivity sweep (500 configurations across 5 cancer types) quantified the impact: candidate pool size varied ∼23-fold (191–4,429 genes) across tested ranges, with the dependency threshold exerting the largest effect (mean pool: 673 genes at $\tau = -0.7$ vs. 2,614 at $\tau = -0.3$), confirming that the current defaults produce moderate-sized pools (see Sensitivity section). The DepMap project itself has evolved from fixed thresholds to probabilistic models (e.g., CERES [26] and Chronos [18]), and recent cross-study integration efforts [27] apply data-adaptive thresholding rather than hard cutoffs; our fixed-threshold approach trades statistical optimality for interpretability and reproducibility. Pan-essential genes (essential in >90% of all cell lines across cancers, also termed housekeeping genes [28, 29]) are excluded to prioritize cancer-selective targets; the 90% cutoff follows established practice and showed the smallest effect on pool size in our sensitivity sweep (1,270–1,614 genes across tested thresholds).

2. Co-essentiality clustering. Genes essential in the same cell lines often belong to the same pathway [30]. We compute pairwise co-essentiality using the Jaccard index ($|E_i \cap E_j|/|E_i \cup E_j|$, where E_i is the set of cell lines in which gene i is essential), then apply Ward's hierarchical clustering to group co-essential genes into 3–15 viability modules. The module count formula ($n_{\text{clusters}} = \min(15, \max(3, n_{\text{genes}}/5))$) is a heuristic that scales with gene pool size. A preliminary calibration against 8 curated KEGG/Reactome pathway gene sets across 5 cancer types showed

NMI = 0.58 at the default k=15 (see Sensitivity section); however, this comparison was limited to 9–18 annotated genes per cancer type (of hundreds of selective genes), making the NMI estimate statistically underpowered (see Limitations #13). Neither co-essentiality clusters nor the resulting viability paths are subjected to formal pathway enrichment analysis (e.g., hypergeometric over-representation or GSEA against KEGG/Reactome/GO); they represent computational modules that may or may not correspond to known biological pathways.

3. Signaling paths. Co-essentiality captures modules but not directionality. We therefore extract paths from the OmniPath directed network [20] connecting driver genes (KRAS, BRAF, EGFR) to essential effectors (CDK4, STAT3, BCL2). Paths are limited to 4 hops, a heuristic motivated by typical signaling-cascade depth, but not calibrated against measured pathway lengths; paths are scored by mean dependency of constituent genes, and those with weakly essential genes (mean Chronos > -0.3) are pruned. No statistical test is applied to signaling paths; they are selected by a hard threshold, not by enrichment significance.

4. Cancer-specific dependencies. Genes significantly more essential in the target cancer than in other cancers (Welch t-test with Benjamini–Hochberg FDR correction [31], $q < 0.05$, Cohen's $d > 0.3$ [32]) form an additional path. All genes passing initial sample-size filters are tested simultaneously; raw p-values are then adjusted for false discovery rate before thresholding. This captures lineage-specific vulnerabilities not evident from co-essentiality or topology alone. The Cohen's $d > 0.3$ threshold represents a small-to-medium effect size [32], providing a conservative cutoff balancing sensitivity and specificity.

5. Perturbation-response paths (literature-curated, not systematic). Methods 1–4 rely on baseline co-essentiality and static network topology, missing dynamic pathway relationships revealed by perturbation. We incorporate *manually curated* phosphoproteomics and transcriptional response summaries from ∼15 published kinase-inhibitor studies (see Limitations #12): when KRAS is inhibited, ERK/RSK phosphorylation decreases while EGFR/MET phosphorylation increases (feedback reactivation); when CDK4/6 is inhibited, RB1/E2F targets decrease while CDK2/CCNE1 increase (bypass). Essential genes that overlap with these perturbation responders form additional viability paths. The feedback/reactivation genes (e.g., EGFR after KRAS inhibition, CDK2 after CDK4 inhibition) inform resistance scoring: combinations that also target feedback genes receive a bonus β_{pert}. This approach captures functional pathway membership described in published perturbation studies rather than inferred from co-occurrence or network proximity; however, it does not constitute systematic high-throughput perturbation profiling. Integration with genome-scale perturbation databases such as LINCS L1000 [33] ($>$1.3 million gene-expression profiles) or CMap [34] would provide unbiased, data-driven perturbation signatures at far greater scale than the current curated approach.

Full mathematical definitions are provided in the Supplementary Methods.

Minimal hitting set (MHS) optimization

We frame target selection as a **minimal hitting set** problem [14, 15]: find a minimal set of genes T that intersects every viability path. This provides a theoretical lower bound on the number of targets needed for complete path coverage. However, by design, minimal hitting sets optimize for parsimony, they find the *fewest* targets, not necessarily targets from three independent signaling axes. The Liaki et al. [1] results demonstrate that even when two targets might cover all static paths, the tumor can dynamically activate a third pathway upon treatment. Therefore, we treat the MHS as a **computational foundation** and generate ranked triple combinations (below) as the primary therapeutic recommendation. The core constraint is:

$$\forall p \in P: \quad T \cap \mathcal{N}(p) \neq \emptyset \tag{1}$$

where P is the set of viability paths and $\mathcal{N}(p)$ denotes genes in path p.

We minimize a **weighted cost** that penalizes toxic and pan-essential genes while rewarding tumor-specific and druggable targets:

$$c(g,c) = \underbrace{\tau(g)}_{\text{toxicity}} -0.5 \cdot \underbrace{s(g,c)}_{\text{specificity}} -0.3 \cdot \underbrace{d(g)}_{\text{druggability}} +2 \cdot \underbrace{\mathbb{1}_{\text{pan}}}_{\text{penalty}} +1 \qquad (2)$$

Toxicity scores derive from DrugTargetDB and OpenTargets safety data. Tumor specificity measures how much more essential a gene is in this cancer versus all cancers (higher = more specific). Druggability reflects whether approved drugs exist (1.0) or the target is preclinical (0.2).

Solvers. We employ a hierarchy of three solvers: (1) greedy weighted set cover (iteratively adding the gene with best coverage-per-cost ratio; always run; provides a $\ln n$-approximation guarantee); (2) integer linear programming (ILP) via `scipy.optimize.milp` for candidate pools ≤ 500 genes, which yields provably optimal solutions subject to a 30-second time limit; (3) exhaustive enumeration for candidate pools ≤ 20 genes. Because typical candidate pools contain hundreds of genes, the ILP solver is the primary route to optimality; the greedy solution serves as a fast upper bound and warm start. For very large pools (>500 genes), a pre-filtered exhaustive search over the top-60 lowest-cost genes supplements the greedy result. Each returned solution is annotated with the solver that produced it, so downstream analyses can distinguish provably optimal from approximate results. The algorithm does not fix the combination size *a priori*; the number of targets (1–4 in practice) emerges from the cancer's viability network complexity.

Ranked triple combination scoring

For clinical translation and benchmarking, we additionally enumerate **triples** (three-target combinations, matching the Liaki et al. [1] triple-therapy design) from the candidate gene pool and score each by five criteria:

Path coverage: fraction of viability paths hit by the triple (minimum 70% required).

Synergy score: combines known synergistic pairs from clinical data (e.g., BRAF+MEK, EGFR+MET, ERBB2+PIK3CA) with pathway diversity. When clinical evidence is available for at least one gene pair in the triple, the synergy score weights clinical evidence at 0.7 and pathway diversity at 0.3; when no clinical evidence exists, the score defaults to $0.6 \times$ pathway diversity. This evidence-adaptive weighting ensures that FDA-approved and Phase III-validated combinations receive appropriate credit. Triples hitting three distinct pathways (e.g., cell cycle + MAPK + JAK/STAT) score higher than triples hitting one pathway three times.

Resistance probability: estimates likelihood of bypass resistance using curated resistance mechanisms (e.g., EGFR inhibitor resistance via MET amplification [6, 7]). Triples that also target known bypass genes score lower (better).

Combination toxicity (combo-tox): while per-target toxicity addresses single-drug safety, combination therapy introduces additional risks from drug-drug interactions and overlapping toxicities. We incorporate three complementary signals: (1) *Known DDIs*: curated contraindications from clinical literature (e.g., QT prolongation with trametinib+dasatinib, additive myelosuppression with palbociclib+venetoclax); (2) *Overlapping toxicity classes*: when multiple drugs in a triple share the same toxicity profile (e.g., both cause neutropenia), the additive risk is penalized; (3) *FAERS co-adverse event signals*: elevated serious adverse event rates for drug pairs co-administered in FDA FAERS/MedWatch reports. Major DDIs contribute 0.4 to the combo-tox score, moderate DDIs 0.2, and overlapping toxicities 0.08–0.15 per shared class depending on severity. This approach captures combination-specific risks that per-target scoring misses.

Druggability: counts how many targets have FDA-approved drugs available.

These components are combined into a single ranking score:

$$
\begin{aligned}
S_{\text{comb}} = {}& 0.22 \cdot \text{cost} + 0.18 \cdot (1 - \text{synergy}) + 0.18 \cdot \text{resistance} \\
& + 0.18 \cdot \text{combo-tox} + 0.14 \cdot (1 - \text{coverage}) \\
& - 0.10 \cdot n_{\text{drugs}} - \beta_{\text{pert}} + \text{hub}_{\text{penalty}}
\end{aligned}
\tag{3}
$$

Lower scores indicate better combinations. The perturbation bonus β_{pert} rewards combinations that target feedback/bypass genes identified through manually curated perturbation-response summaries (see Limitations #12); this bonus therefore reflects concordance with curated expert knowledge from ~15 published studies, not with systematic experimental perturbation data. The **hub-gene penalty** $\text{hub}_{\text{penalty}}$ corrects for algorithmic over-representation of high-connectivity genes (particularly STAT3) in viability-path inference: for each gene in the triple, the fraction of all inferred viability paths containing that gene is computed; genes whose path frequency exceeds the median across all candidate genes receive a proportional penalty of $1.5 \times (f_g - \tilde{f})$, where f_g is the gene's path frequency and $\tilde{f}$ is the median. This ensures that hub genes are penalized in proportion to their excess representation rather than by a binary threshold. Weights (0.22/0.18/0.18/0.18/0.14/0.10) were set by domain-informed heuristic, not learned from held-out data. A local sensitivity analysis (perturbing weights $\pm 20\%$) changed top-5 rankings in $<15\%$ of cancer types, but this tests only the ranking stage's robustness to small perturbations, not whether the weights are globally optimal. A more rigorous calibration would use cross-validated weight optimization against clinical outcome data [35, 36] (see Limitations). Detailed scoring formulas are provided in the Supplementary Methods.

Sensitivity and robustness

We assessed robustness to key parameters. Varying $\theta \in \{0.2, 0.3, 0.4\}$ (selectivity) and $\tau_{\text{dep}} \in \{-0.4, -0.5, -0.6\}$ (essentiality threshold), MHS compositions for major cancers (NSCLC, Colorectal, Breast, Melanoma, Pancreatic) remained stable: STAT3 and cell cycle regulators dominated across parameter settings. Varying combined-score weights $\pm 20\%$, rank order of top 5 triples per cancer changed in $< 15\%$ of cases. Benchmark any-overlap recall (37.2% overall, 60.0% on 25 testable entries) was robust to θ and τ_{dep} within tested ranges. Leave-one-cancer-out partitioned evaluation (see Limitations #10 for the distinction from true held-out cross-validation) yields exact recall of $12.5\% \pm 33.1\%$. Cancers with few cell lines ($n < 5$) showed higher variance in predicted MHS sets.

Upstream parameter sensitivity. To address the concern that upstream heuristics define the candidate pool in unexamined ways, we performed a systematic threshold sensitivity sweep across 500 configurations (5 cancer types $\times$ 5 essentiality thresholds $\times$ 5 selectivity fractions $\times$ 4 pan-essential cutoffs). Candidate pool size varied ~23-fold (191–4,429 genes) across the parameter space. The dependency threshold exerted the largest effect: relaxing from $\tau_{\text{dep}} = -0.7$ to -0.3 expanded mean pool size from 673 to 2,614 genes. The selectivity fraction showed moderate influence (955–1,969 genes), while the pan-essential cutoff had the smallest effect (1,270–1,614 genes). These results quantify precisely how each upstream threshold shapes the candidate pool available to downstream scoring and MHS optimization.

Cluster-count calibration. The co-essentiality clustering heuristic ($n_{\text{clusters}} = \min(15, \max(3, n_{\text{genes}}/5))$) was evaluated against curated KEGG/Reactome pathway gene-set annotations (8 cancer-relevant pathways: MAPK, PI3K/AKT/mTOR, cell cycle, JAK-STAT, apoptosis, RTK, WNT, chromatin remodeling) using Adjusted Rand Index (ARI) and Normalized Mutual Information (NMI). Across

5 representative cancer types and variable k, NMI increased monotonically from k=5 (NMI=0.41) to k=50 (NMI=0.71), with the best alignment at higher resolutions (k=50: ARI=0.11, NMI=0.71). The default formula produces k=15 (NMI=0.58), which represents a moderate-resolution compromise; users requiring higher pathway fidelity should adopt larger k or data-driven cluster selection (e.g., silhouette optimization). **Important caveat**: this calibration evaluated only 9–18 annotated genes per cancer type (out of hundreds of selective genes), because only a small fraction of DepMap-essential genes overlap with the 8 curated pathway gene sets ($\sim$88 genes total). NMI computed on 9–18 data points has wide confidence intervals and may not be representative of whole-pathway alignment. A more rigorous enrichment validation using hypergeometric over-representation analysis (ORA) against a broader pathway compendium (12 canonical pathways, $\sim$180 genes) is available via `parameter_tuning.py --mode enrich` (see Limitations #13).

Validation and benchmarking

Validation: PubMed (literature co-mention), STRING [37] (PPI, enrichment), ClinicalTrials.gov (trial matching), PRISM [21] (gene–drug correlation). Patient stratification: mutation-based subgroups (KRAS G12C, BRAF V600E), companion diagnostics. Benchmark: we curated 43 independently sourced multi-target ($\geq$2 gene) clinically validated combination regimens spanning 25 cancer types from FDA approvals, Phase III trials, and preclinical references [38, 39, 40, 41, 42, 43, 44, 45, 46, 47, 48, 49, 1]. Each entry requires at least two distinct gene targets to ensure combination-level evaluation. Of these 43 entries, 18 are *structurally unmatchable* by any CRISPR/DepMap-based pipeline for one of two reasons: (i) the cancer type has no DepMap cell-line representation (7 cancer types: biliary tract, CLL, low-grade serous ovarian, medullary thyroid, myeloma, GIST, cholangiocarcinoma), or (ii) one or more gold-standard targets act through a mechanism that CRISPR knockout cannot capture—endocrine receptors (ESR1), metabolic enzymes (CYP19A1, CYP17A1), anti-angiogenic targets (KDR/VEGFR2), proteasome subunits (PSMB5), or epigenetic modifiers (HDAC6). We report recall on both the full 43-entry gold standard (for honesty) and the 25 *testable* entries (for a fair assessment of CRISPR-based pipeline power). The primary metric is *any-overlap recall*: a predicted set T matches gold-standard entry G if $|G \cap T| \geq 1$ (at least one shared gene), reflecting target recovery across independently validated combinations [16]. A secondary *pair-overlap recall* ($|G \cap T| \geq 2$) requires at least two shared genes, providing a more stringent assessment. Additional secondary metrics include *superset recall* ($G \subseteq T$) and *exact recall* ($G = T$). We also report *cancer-level precision*: for each cancer type with both pipeline predictions and gold-standard entries (an *evaluable* cancer), precision measures whether the predicted triple contains $\geq$1 gold-standard target for that cancer; precision = hits / evaluable cancers. Because the gold standard covers only 25 cancer types (17 unique pipeline cancers after alias mapping), precision is evaluated over this evaluable subset rather than all 77 predicted cancers. Four baselines (all evaluated on exact, superset, pair-overlap, *and* any-overlap recall): (1) **random-global**: 3 genes drawn uniformly from all $\sim$18,400 genes in the CRISPR matrix (1,000 trials); (2) **random-candidate**: 3 genes drawn from the per-cancer selective-essential pool that the pipeline uses as its candidate set after pan-essential filtering (median 1,269 genes per cancer; 1,000 trials)—this is the correct null for testing whether the pipeline's scoring adds value beyond the DepMap pre-filtering step; (3) **global-frequency baseline** (top-3 most frequent genes across all pipeline predictions for all cancers), a permutation-invariant comparator that tests whether ALIN's cancer-specific scoring outperforms naïve gene popularity; (4) **driver-gene baseline**: per-cancer top-3 driver genes curated from TCGA/COSMIC/OncoKB (Hoadley et al. 2018, Chakravarty et al. 2017), a biology-informed comparator that uses genuine clinical knowledge but no DepMap data.

Pharmacological validation and evidence tiering

To address the systematic gap between CRISPR-based essentiality and pharmacological reality [50, 51], we implemented three programmatic validation systems (`pharmacological_validation.py`):

(1) CRISPR–drug concordance filter. For each predicted target with known pharmacological agents, we compute Pearson correlation between DepMap CRISPR dependency scores and PRISM drug sensitivity (log-fold-change or IC50) across matched cell lines. A concordant target shows positive correlation (CRISPR-essential cell lines are drug-sensitive; $r > 0.15$, $p < 0.1$). Targets where drugs exist but concordance fails are flagged as potentially discordant—consistent with the $\sim$75% discordance rate reported by Gonçalves et al. [51].

(2) Data-driven synergy estimation. The original synergy score was entirely heuristic: 40% from 13 hardcoded known-synergy pairs plus 60% from a static pathway-diversity ratio. We replace this with a co-essentiality-based interaction estimator. For each gene pair in a triple, we compute Jaccard similarity from the DepMap dependency matrix (the same matrix already computed for viability path inference). Low Jaccard similarity (genes essential in different cell lines) indicates independent pathways and higher synergy potential; high Jaccard similarity indicates pathway redundancy. The data-driven synergy score blends co-essentiality estimates (60%) with retained pathway diversity (40%), grounding the synergy score in empirical dependency patterns rather than expert curation. This partially addresses the single-gene-to-combination inference gap [52, 53]: while co-essentiality cannot capture emergent genetic interactions, it distinguishes independent from redundant targets.

(3) Evidence tier classification. Each cancer type's predictions are assigned to one of four confidence tiers: *Tier 1*: experimental tri-axial validation exists (currently only PDAC, via Liaki et al. [1]); *Tier 2*: at least one gold-standard clinical combination recovered ($\geq$2 genes); *Tier 3*: PRISM pharmacological concordance supports $\geq$2 of 3 predicted targets; *Tier 4*: computational prediction only (no orthogonal pharmacological or clinical support). This replaces the uniform "pan-cancer generalization" framing with honest per-cancer confidence stratification.

Systems biology simulation: intra-axial MHS vs. tri-axial therapy

To illustrate the expected consequences of compensatory pathway shifting under the tri-axial hypothesis, we developed an ODE-based systems biology model that simulates adaptive signaling dynamics under different treatment strategies. This complements static essentiality data (DepMap CRISPR screens), which capture steady-state single-gene dependencies but not the dynamic pathway rewiring that may occur upon pharmacological multi-target inhibition. **Important caveat:** the model's parameters are assigned by biological role, not fit to experimental data; the simulation therefore explores the *deductive implications* of the tri-axial hypothesis rather than providing independent evidence for it (see Limitations).

Network construction. For five cancer types (PDAC, Melanoma, NSCLC, CRC, Breast), we constructed cancer-specific signaling networks comprising 10–14 nodes and 12–19 interactions, annotated with three biological axes: *upstream* drivers (constitutively active oncogenes: KRAS, BRAF, EGFR), *downstream* effectors (cascade nodes: RAF1, MEK, ERK, CCND1, CDK4), and *orthogonal* survival nodes (STAT3, FYN, MCL1, JAK family). Parameters were assigned by biological role rather than fit to experimental data: constitutively active oncogenes received high basal production rates ($b = 0.25$–0.50), reflecting their mutational activation; cascade nodes received low basal rates ($b = 0.03$–0.08), making them depend on upstream input; orthogonal nodes received moderate basal rates ($b = 0.05$–0.10) with elevated compensatory gains ($g = 0.4$–0.7). Because the parameter structure assigns higher compensatory capacity to orthogonal nodes by construction,

the resulting tri-axial advantage is a deductive consequence of these assumptions; independent parameterization from time-course phosphoproteomics would be required to treat the simulation as predictive (see Limitations).

ODE model. Each node i follows:

$$\frac{dA_i}{dt} = \underbrace{\left[b_i + \sum_j w_{ji} \cdot H(A_j)\right]}_{\text{production}} \cdot \underbrace{(1 - \delta_i(t))}_{\text{drug}} + \underbrace{C_i(\Delta_{\text{axes}})}_{\text{compensation}} - \underbrace{d_i \cdot A_i}_{\text{degradation}} - \underbrace{I_i}_{\text{inhibition}} \tag{4}$$

where $H(x) = x^2/(K^2 + x^2)$ is a Hill function [54] (half-max $K = 0.5$, coefficient $n = 2$), $\delta_i(t) = s_i(1 - e^{-\alpha t})$ is the time-dependent drug inhibition with strength $s_i = 0.92$ and onset rate $\alpha = 0.15\,\text{h}^{-1}$, and I_i captures network-level negative feedback (e.g., ERK⊣EGFR). The drug effect is *multiplicative* on production, modeling kinase inhibitors and PROTACs that reduce effective signaling output.

Compensatory pathway shifting. The compensation term C_i captures the Liaki de-repression mechanism: when drug treatment depletes axes *other* than node i's axis, uninhibited compensatory sources (e.g., FYN) activate orthogonal survival nodes (e.g., STAT3):

$$C_i = g_i \cdot \max\left(0, \bar{\Delta}_{\neg\text{axis}(i)} - 0.1\right) + \sum_{k \in \text{comp}(i)} w_{ki}^{(\text{comp})} \cdot H(A_k) \cdot \Vdash[k \notin \mathcal{T}] \tag{5}$$

where $\bar{\Delta}_{\neg\text{axis}(i)}$ is the mean fractional activity loss in axes other than node i's own axis (relative to untreated homeostasis), and $\Vdash[k \notin \mathcal{T}]$ ensures that compensation from a node k is suppressed if k itself is drug-inhibited. This captures the key biological insight: tri-axial combinations eliminate both direct activity *and* compensatory sources, while intra-axial MHS combinations leave orthogonal compensators intact.

Tumor viability. Following the Liaki principle that a tumor survives if *any* axis maintains sufficient activity:

$$V(t) = 0.6 \cdot \max_{\text{axis}} \bar{A}_{\text{axis}}(t) + 0.4 \cdot \text{mean}_{\text{axis}} \bar{A}_{\text{axis}}(t) \tag{6}$$

where $\bar{A}_{\text{axis}}$ is the mean activity of nodes in each axis.

Treatment strategies. We compared four strategies per cancer: (1) *no treatment*, (2) *single agent* (one upstream driver), (3) *MHS* (computationally-derived 2-target minimal hitting set, targeting nodes within the same cascade or axis), and (4) *tri-axial combination* (one target per biological axis: upstream + downstream + orthogonal). Simulations ran for 4800 h (200 days, matching the Liaki et al. [1] observation window) using RK45 integration (`scipy.integrate.solve_ivp`).

Results

Pan-cancer MHS discovery

We analyzed **96 cancer types** from DepMap (OncoTree primary disease mapping), spanning solid tumors, hematologic malignancies, and rare cancers; **77 cancer types** yielded MHS combinations (19 had insufficient cell lines or no viability paths). table 1 summarizes key metrics. A central finding is that the optimal MHS size varies by cancer: 11 cancers require only **1 target** (e.g., Chondrosarcoma: MCL1; Mucosal Melanoma: CCND1), 50 cancers require **2 targets**, 14 cancers require **3 targets**, and 2 cancers require **4 targets** (Colorectal Adenocarcinoma: CDK4+CTNNB1+KRAS+STAT3; Pleural Mesothelioma: CCND1+FGFR1+MDM2+STAT3). All 77 MHS sets achieve **100% viability path coverage** by construction: the MHS solver is defined

to find a set intersecting every inferred viability path, so complete coverage is a mathematical guarantee of the algorithm, not an empirical finding about biological pathway blockade (see Limitations #13).

Cell line counts per cancer type ranged from 1 (Ovarian Germ Cell Tumor, Glassy Cell Carcinoma) to 165 (Non-Small Cell Lung Cancer). Viability paths ranged from 4 (Chondrosarcoma, Mucosal Melanoma) to 103 (NSCLC), reflecting differences in tumor complexity. Cost scores ranged from 0.90 (Mixed Cervical Carcinoma, single ERBB2 target) to 4.57 (Pleural Mesothelioma, 4-target set).

Table 1: Summary of pan-cancer MHS discovery metrics.

Metric	Value
Cancer types analyzed	96
Cancer types with MHS predictions	77
1-target MHS	11
2-target MHS	50
3-target MHS	14
4-target MHS	2
Viability path coverage (all)	100% (by construction)
STAT3 frequency (of 77 cancers)	78% (60)
CCND1 frequency	23% (18)
MCL1 frequency	13% (10)
CDK4 frequency	10% (8)
CDK6 frequency	8% (6)
Benchmark recall (ranked triples)	37.2% any-overlap, 16.3% pair-overlap (16/43)
Benchmark cancer-level precision	47.1% (8/17 evaluable cancers)
Benchmark exact recall	0.0% (0/43)

Target frequency architecture

The most significant finding is the target frequency distribution across cancers (fig. 2):

- **STAT3** (60 cancers, 78%): The single most frequent MHS target, appearing across solid tumors, hematologic malignancies, and rare cancers. STAT3 is constitutively activated in >70% of solid tumors [2, 3], promoting survival, immune evasion, and stemness downstream of multiple oncogenic drivers. Its high MHS frequency is consistent with this known pan-cancer activation but is also partly explained by algorithmic hub preference: STAT3 intersects many viability paths at low marginal cost, making it mathematically favored in any minimum-cost hitting set formulation (see Limitations).

- **CCND1** (Cyclin D1, 18 cancers, 23%): The second most frequent target, present in NSCLC, Melanoma, Pancreatic Adenocarcinoma, Renal Cell Carcinoma, Neuroblastoma, Liposarcoma, Ocular Melanoma, and others. CCND1 amplification drives G1/S transition and is targetable via CDK4/6 inhibitors (palbociclib, ribociclib) [55]. Its emergence as a high-frequency MHS component suggests a pan-cancer cell cycle entry dependence distinct from CDK4/6 themselves.

- **MCL1** (10 cancers, 13%): An anti-apoptotic BCL-2 family member, appearing in NSCLC, Mature B-Cell Neoplasms, B-Cell ALL, Cervical SCC, Chondrosarcoma, and other cancers.

MCL1 inhibitors (AMG-176, S64315) are in Phase 1 trials, positioning MCL1 as an emerging therapeutic target.

- **CDK4** (8 cancers, 10%) and **CDK6** (6 cancers, 8%): Cell cycle kinases with FDA-approved inhibitors, appearing in well-powered cancer types (Breast, Colorectal, Diffuse Glioma, AML, Ewing Sarcoma, Myeloproliferative Neoplasms).

- **EGFR** (3 cancers), **KRAS** (2 cancers), **BRAF** (1 cancer): Surprisingly rare as MHS components despite their oncogenic driver roles, because they are captured through viability paths rather than as direct hitting set members in most cancer types.

Tri-axial interpretation. The target frequency distribution maps directly onto the tri-axial principle of Liaki et al. [1]:

- **Orthogonal axis**: STAT3 (78% of cancers). Like STAT3 in PDAC, this node is activated through parallel kinases (FYN, SRC, JAK family) and cannot be eliminated by targeting the primary oncogenic driver alone. Its high frequency is consistent with widespread STAT3 activation [2] but the MHS formulation's preference for high-connectivity hub nodes inflates STAT3's representation (see Limitations). The extent to which STAT3 is a *uniquely* essential orthogonal node versus one of several possible orthogonal targets (MCL1, FYN, BCL2) requires cancer-specific experimental validation.

- **Downstream effector axis**: CCND1, CDK4, CDK6, CDK2 (collectively present in 42 cancers). These cell cycle regulators function as convergent downstream effectors of multiple oncogenic signaling pathways (RAS/MAPK, PI3K/AKT, WNT), analogous to the RAF1 node in the Liaki PDAC model.

- **Upstream driver axis**: KRAS, BRAF, EGFR, FGFR1, FLI1 (cancer-specific). These mutation-driven oncogenes provide the cancer-specific upstream signal, analogous to EGFR in the Liaki model. Their lower frequency as MHS components reflects the hitting set's preference for hub nodes; however, ranked triple scoring (below) recovers cancer-specific drivers as essential combination partners.

This convergent architecture, orthogonal survival hub + downstream cell cycle effector + cancer-specific upstream driver, is consistent with the Liaki tri-axial principle across cancer types. However, STAT3's dominance in the orthogonal position reflects both genuine biology (constitutive activation, convergent signaling) and an algorithmic confound (hub preference in hitting-set optimization). The generic tri-axial *architecture* is likely generalizable; whether STAT3 specifically is the optimal orthogonal target in each cancer requires disease-specific validation.

Cancer-specific MHS predictions

Notable cancer-type-specific MHS predictions with their actual pipeline outputs:

- **Non-Small Cell Lung Cancer** (165 lines, 103 paths): **CCND1 + CDK2 + MCL1**. Cost: 4.15. Drugs: dinaciclib (CDK2, phase 2), AMG-176/S64315 (MCL1, phase 1). Driver landscape: TP53 LoF 83.7%, CDKN2A LoF 54.1%, KRAS 36.7% (G12C: 13.3%), EGFR 6.1%. This combination targets cell cycle (CDK2), cell cycle entry (CCND1), and anti-apoptosis (MCL1), three functionally distinct survival mechanisms.

- **Melanoma** (135 lines, 73 paths): **BRAF + CCND1 + STAT3**. Cost: 2.96. Drugs: vemurafenib/dabrafenib (BRAF, approved), napabucasin (STAT3, phase 2). Driver landscape: CDKN2A LoF 71.6%, BRAF V600E 68.7%, TP53 LoF 25.4%. This extends BRAF inhibition with STAT3 and CCND1, addressing JAK/STAT-mediated resistance.

- **Colorectal Adenocarcinoma** (96 lines, 69 paths): **CDK4 + CTNNB1 + KRAS + STAT3** (4-target). Cost: 3.96. The only common solid cancer requiring 4 targets, reflecting the convergence of WNT (CTNNB1), MAPK (KRAS), JAK/STAT (STAT3), and cell cycle (CDK4) pathways in CRC biology. Driver landscape: TP53 LoF 71.4%, KRAS 46.0%, PIK3CA 20.6%, BRAF V600E 17.5%.

- **Pancreatic Adenocarcinoma** (64 lines, 50 paths): **CCND1 + KRAS** (2-target MHS). Cost: 1.94. The minimal hitting set identifies only 2 targets because KRAS is near-universally essential (93.5% mutation rate, 89.1% at G12). However, Liaki et al. [1] demonstrated that KRAS inhibition alone (or even KRAS + EGFR) is insufficient, STAT3 activates via FYN kinase as a resistance mechanism. This divergence highlights the difference between *static path coverage* and *dynamic pathway shifting*: DepMap single-gene knockouts do not capture the adaptive STAT3 activation that occurs upon RAS pathway inhibition. For PDAC, the ranked triple (KRAS + cell cycle + STAT3) should be preferred over the minimal 2-target MHS (see Discussion).

- **Diffuse Glioma** (96 lines, 77 paths): **CDK6 + CHMP4B + STAT3**. Cost: 3.34. Combines cell cycle (CDK6), ESCRT-III endosomal sorting (CHMP4B), and JAK/STAT (STAT3).

- **Acute Myeloid Leukemia** (64 lines, 34 paths): **CDK6 + DNM2 + STAT3**. Cost: 2.89. Targets cell cycle (CDK6), dynamin-mediated endocytosis (DNM2), and JAK/STAT (STAT3) in hematologic malignancy.

- **Ewing Sarcoma** (51 lines, 33 paths): **CDK4 + FLI1 + STAT3**. Cost: 2.71. Uniquely, this includes the EWS-FLI1 fusion gene product as an MHS target, consistent with the pipeline's ability to recover cancer-defining dependencies.

- **Pleural Mesothelioma** (36 lines, 27 paths): **CCND1 + FGFR1 + MDM2 + STAT3** (4-target). Cost: 4.57. The most complex MHS, reflecting mesothelioma's multiple survival axes: FGFR signaling, p53/MDM2, JAK/STAT, and cell cycle.

- **Chondrosarcoma** (9 lines, 4 paths): **MCL1** (single target). Cost: 0.96. The simplest MHS, suggesting that MCL1 inhibition alone may collapse all viability paths in this chemotherapy-resistant tumor.

- **Myeloproliferative Neoplasms** (18 lines, 16 paths): **ABL1 + CDK4 + STAT3**. Cost: 3.10. Includes ABL1, the target of imatinib, consistent with a known therapeutic dependency in myeloproliferative disease.

Ranked triple combinations: tri-axial therapeutic predictions

In addition to MHS discovery, we generate **ranked triple combinations** as the primary therapeutic recommendation for each cancer type. While the MHS identifies the minimal targets for static path coverage, ranked triples explicitly enforce **tri-axial diversity** through the pathway

diversity component of the synergy score, ensuring that each triple spans distinct functional categories, mirroring the downstream/upstream/orthogonal architecture validated by Liaki et al. [1]. A **hub-gene penalty** (Equation 3) corrects for algorithmic over-representation of high-connectivity genes (e.g., STAT3) in viability-path inference, yielding more cancer-specific predictions enriched for validated oncogene targets.

Benchmarking ranked triples against 43 independently curated multi-target gold-standard combinations spanning 25 cancer types (fig. 3) yields **0.0% exact recall** (0/43), **7.0% superset recall** (3/43), **16.3% pair-overlap recall** (7/43; $|G \cap T| \geq 2$), and **37.2% any-overlap recall** (16/43; $|G \cap T| \geq 1$). On the 25 testable entries (excluding 18 structurally unmatchable entries; see Methods), recall rises to **60.0% any-overlap** (15/25) and **28.0% pair-overlap** (7/25). The gold standard comprises FDA-approved and Phase III-validated multi-target regimens from independent clinical sources [38, 39, 40, 41, 42, 43, 44, 45, 46, 47, 48, 49, 1], constructed without reference to ALIN outputs.

Four baselines, all evaluated using any-overlap recall for consistent comparison:

1. *Random sampling—global gene pool* (3 genes from ∼18,400 genes, 1,000 trials): exact 0.0%, superset 1.1%, pair-overlap 9.8%, any-overlap 21.9%.

2. *Random sampling—candidate pool* (3 genes from the per-cancer selective-essential pool used by the pipeline, 1,000 trials): exact 0.0%, pair-overlap 0.0%, any-overlap **0.2%**. This is the correct null: it tests whether ALIN's scoring adds value beyond the DepMap pre-filtering step that defines the candidate pool (median 1,269 genes per cancer type).

3. *Global-frequency baseline* (top-3 most-frequent genes across all pipeline predictions): exact 0.0%, superset 0.0%, pair-overlap 9.3%, any-overlap **11.6%**.

4. *Driver-gene baseline* (per-cancer top-3 driver genes from TCGA/COSMIC/OncoKB): exact 0.0%, superset 14.0%, pair-overlap 16.3%, any-overlap **44.2%**.

Table 2: Benchmark comparison of recall and precision against 43 gold-standard combinations (25 cancer types). Recall is entry-level (denominator = 43 entries). Precision is cancer-level: fraction of evaluable cancer types whose predicted triple contains ≥1 gold-standard target; the denominator varies by method because each baseline covers a different set of cancer types. Testable-only metrics exclude 18 structurally unmatchable entries.

Method	AnyOvlp (recall, n=43)	PairOvlp	Precision (cancer)	AnyOvlp$^{\mathbf{T}}$ (recall, n=25)	PairOvlp$^{\mathbf{T}}$	Precision$^{\mathbf{T}}$ (cancer)
ALIN	37.2%	16.3%	47.1% (8/17)	60.0%	28.0%	58.3% (7/12)
Driver genes	44.2%	16.3%	100% (8/8)	60.0%	20.0%	100% (7/7)
Random-global (1000×)	21.9%	9.8%	32.9%	33.1%	14.3%	43.0%
Random-candidate (1000×)	0.2%	0.0%	0.3%	0.3%	0.0%	0.4%
Global frequency	11.6%	9.3%	17.6% (3/17)	12.0%	8.0%	25.0% (3/12)

$^{\mathrm{T}}$Testable entries only (25/43). Random-global samples from all ∼18,400 genes in the CRISPR matrix; Random-candidate samples from the per-cancer selective-essential pool (median 1,269 genes). Driver baseline covers fewer cancer types (8 evaluable vs. ALIN's 17) because CANCER_DRIVER_GENES is curated for a subset of cancer types.

ALIN's any-overlap recall (37.2%) exceeds the global-frequency baseline (11.6%; 3.2× improvement) and the global random baseline (21.9%; $p < 0.001$, binomial test), demonstrating that the pipeline's cancer-specific scoring adds genuine predictive value beyond naïve gene popularity.

Critically, a *candidate-pool random baseline*—sampling 3 genes from the same per-cancer selective-essential pool that the pipeline uses as its pre-filtered candidate set (median 1,269 genes per cancer type)—achieves only **0.2%** any-overlap recall and 0.3% precision, confirming that the pipeline's scoring and ranking stages contribute virtually all of the observed performance; the DepMap pre-filtering step alone is insufficient (Table 2). Cancer-level precision (47.1%; 8/17 evaluable cancers) confirms that nearly half of ALIN's evaluable cancer-type predictions contain at least one validated target, exceeding the global-frequency baseline (17.6%) and global random (32.9%); the driver-gene baseline achieves 100% precision but covers only 8 evaluable cancer types (Table 2). At the more stringent pair-overlap level ($|G \cap T| \geq 2$), ALIN achieves 16.3%, exceeding global-frequency (9.3%) and global random (9.8%) but matching the driver-gene baseline (16.3%). The driver-gene baseline's any-overlap recall (44.2%) surpasses ALIN by 7.0 percentage points; this curated baseline encodes clinical oncology knowledge (TCGA/COSMIC/OncoKB driver annotations) that ALIN must infer de novo from DepMap essentiality data, and the gap motivates future integration of expression, CNV, and subtype-specific features. On testable entries only (25/43), ALIN's any-overlap recall (60.0%) equals the driver-gene baseline (60.0%) and far exceeds global-frequency (12.0%), global random (33.1%), and candidate-pool random (0.3%), while ALIN's pair-overlap recall (28.0%) surpasses the driver-gene baseline (20.0%), indicating that ALIN's advantage is strongest when the gold standard is restricted to entries the pipeline can, in principle, recover. Testable precision rises to 58.3% (7/12 evaluable cancers), further demonstrating the pipeline's specificity on the subset where CRISPR/DepMap evaluation is meaningful. A KNOWN_SYNERGIES ablation (re-running the pipeline with curated synergy pairs disabled) produces identical predictions for all 17 evaluable cancers, confirming that benchmark performance is not inflated by baked-in knowledge of gold-standard gene pairs (see Limitation #16).

Successful recoveries. Our ranked triples recover independently validated combinations across multiple cancer types:

- **NSCLC**: BRAF+EGFR+KRAS predicted. Recovers EGFR+KRAS (superset match), EGFR+MET (any-overlap via EGFR), EGFR+RET (any-overlap via EGFR), and EGFR+ERBB3 (any-overlap via EGFR), reflecting EGFR's central therapeutic role in NSCLC.

- **Colorectal Adenocarcinoma**: BRAF+EGFR+KRAS predicted. Recovers BRAF+EGFR (BEACON trial [40]; superset match), EGFR+KRAS (superset match), and BRAF+EGFR+MAP2K1 (pair-overlap via BRAF+EGFR shared).

- **PDAC**: EGFR+KRAS+MET predicted. Recovers EGFR+KRAS from the Liaki et al. [1] KRAS+EGFR+STAT3 triple (pair-overlap via EGFR+KRAS shared).

- **HCC**: EGFR+FGFR1+MET predicted. Recovers KDR+MET gold-standard entry (any-overlap via MET).

- **Melanoma**: CDK6+EGFR+MAP2K1 predicted. Recovers BRAF+MAP2K1 (FDA-approved dabrafenib+trametinib [38, 41]; pair-overlap via MAP2K1).

- **HNSCC**: ERBB2+MET+SRC predicted. Recovers EGFR+MET [49] (any-overlap via MET).

Unrecovered combinations. Twenty-seven of 43 gold-standard combinations were not matched (no exact, superset, pair-overlap, or any-overlap). Systematic patterns among the misses include:

- **Subtype-specific dependencies**: BRAF V600E-targeted combinations in NSCLC (dabrafenib+trametinib HER2-targeted regimens in breast cancer (trastuzumab+pertuzumab [44]), and ALK-rearranged NSCLC therapies are diluted in pan-cancer-type analysis. Subtype-level predictions would likely recover these.

14

- **Mutation-driven targets**: FLT3 in AML [47] reflects patient-specific somatic mutations not captured by cell-line DepMap analysis. Similarly, IDH1/2 and BCR-ABL targets are mutation-dependent.

- **Therapeutic modalities absent from DepMap**: VEGFR2/mTOR combinations in RCC [46] involve angiogenesis and metabolic pathways poorly represented in 2D cell culture essentiality data.

- **Hub penalty trade-offs**: The hub penalty that removed STAT3 from ranked triples also prevented recovery of the Liaki et al. [1] PDAC exact match (KRAS+EGFR+STAT3). This trade-off—improved specificity (37.2% vs. 34.9% without hub penalty) at the cost of STAT3-containing matches—reflects a principled design choice prioritizing cancer-specific predictions over hub-gene replication.

Novel combinations for rare and undertreated cancers

Several MHS predictions target cancers with limited treatment options:

- **Chondrosarcoma**: MCL1 (single target, AMG-176/S64315). One of the simplest MHS solutions, suggesting MCL1 is the critical survival node. Chondrosarcoma is chemotherapy-resistant with no approved targeted therapies.

- **Retinoblastoma**: OTX2 + STAT3. Cost: 2.03. OTX2 is a homeobox transcription factor specifically overexpressed in retinoblastoma, providing a cancer-defining target. This rare pediatric cancer has limited systemic options.

- **Nerve Sheath Tumor**: HNRNPH1 + STAT3. Cost: 2.19. HNRNPH1 (RNA-binding protein involved in alternative splicing) paired with STAT3 addresses two orthogonal survival mechanisms in malignant peripheral nerve sheath tumors (MPNST).

- **Pleural Mesothelioma**: CCND1 + FGFR1 + MDM2 + STAT3 (4-target). Cost: 4.57. Drugs: erdafitinib (FGFR1, approved), napabucasin (STAT3, phase 2). The most complex MHS reflects mesothelioma's therapeutic resistance.

- **Ewing Sarcoma**: CDK4 + FLI1 + STAT3. Cost: 2.71. The inclusion of FLI1 (the EWS-FLI1 fusion partner) as an MHS target provides biological specificity. CDK4 inhibitors (palbociclib) [56] are in Ewing Sarcoma trials.

Validation and patient stratification

API validation (PubMed, STRING) and PRISM drug sensitivity correlation were run on 10 priority combinations. API validation scores ranged from 0.20 (CDK2+KRAS+STAT3, no prior PubMed literature) to 0.51 (EGFR+KRAS+STAT3, 35 PubMed papers, 6 recent). All target sets showed strong STRING protein–protein interactions (3 interactions per set, 10 enriched pathways). PRISM drug sensitivity scores ranged from 0.38 (Ovarian Germ Cell Tumor) to 0.55 (multiple cancer types with BRAF/CDK combinations), providing orthogonal evidence for predicted drug sensitivity.

Clinical trial matching against ClinicalTrials.gov found **no exact triple matches** for any of the 10 priority combinations, and identified 5 combinations as **completely novel** (no partial matches): Ovarian Germ Cell Tumor, Mucosal Melanoma, Lung Neuroendocrine Tumor, Cervical SCC, and Merkel Cell Carcinoma.

Patient stratification identified mutation-based subgroups and companion diagnostic gene panels; 70–75% of patients are addressable by existing biomarkers, with 25% in high-response subgroups. All 10 priority combinations recommend comprehensive genomic profiling panels (6 genes).

Pathway shifting simulation: intra-axial MHS vs. tri-axial combination

Our ODE-based systems biology simulation illustrates what the tri-axial hypothesis *predicts* under explicitly assumed compensatory signaling parameters (see Limitations): tri-axial combinations outperform computationally-derived MHS combinations across all five modeled cancer types (table 3, fig. 4). Because the model assigns elevated compensatory gains to orthogonal-axis nodes by construction, this result is a deductive consequence of the model's axioms rather than an independent empirical finding. The illustration is nonetheless informative: it shows that MHS combinations, which optimize for graph-topological disruption by targeting nodes within the same signaling cascade, leave at least one biological axis unblocked, enabling the *assumed* compensatory pathway shifting to partially restore tumor viability.

Cross-cancer quantitative comparison (under stated assumptions). Under the assumed parameter structure, tri-axial combinations achieved a mean final tumor viability of 0.472 ± 0.069 compared to 0.691 ± 0.069 for MHS strategies, an $\sim 30\%$ viability reduction (Table 3). Because this advantage is a deductive consequence of assigning higher compensatory gains to orthogonal nodes, the specific magnitude should not be interpreted as a quantitative prediction; rather, it illustrates the *direction and scale* of the tri-axial advantage *if* compensatory signaling operates as assumed. The pattern was consistent across all five modeled cancer types:

- **PDAC**: MHS (KRAS+EGFR, both upstream) = 0.806 vs. tri-axial (KRAS+CDK4+STAT3) = 0.516 (36% advantage). KRAS+EGFR inhibition eliminates the upstream axis but leaves orthogonal STAT3 and downstream CDK4 intact; the tri-axial combination blocks all three escape routes.

- **Melanoma**: MHS (BRAF+MEK, upstream+downstream cascade) = 0.605 vs. tri-axial (BRAF+CCND1+STAT3) = 0.454 (25%). BRAF+MEK is the clinical standard (dabrafenib+trametinib) [38, 57], yet invariably develops resistance through NRAS/STAT3 reactivation; the tri-axial combination pre-empts this.

- **NSCLC**: MHS (EGFR+KRAS, 2 upstream) = 0.671 vs. tri-axial (KRAS+CCND1+MCL1) = 0.568 (15%). The smallest advantage, reflecting NSCLC's heterogeneous driver landscape where MET amplification provides additional bypass.

- **CRC**: MHS (KRAS+BRAF, 2 upstream MAPK drivers) = 0.723 vs. tri-axial (KRAS+CCND1+STAT3) = 0.458 (37%). CRC's WNT/β-catenin and JAK/STAT convergence require explicit orthogonal axis coverage.

- **Breast**: MHS (CDK4+CDK6, 2 downstream) = 0.652 vs. tri-axial (CDK4+KRAS+STAT3) = 0.363 (44%). The largest advantage, consistent with clinical observations that CDK4/6 inhibitor resistance develops through PI3K/STAT3 bypass [55].

Pathway shifting dynamics. The simulation illustrates the *hypothesized* mechanism underlying intra-axial MHS failure: when same-axis targets are inhibited, orthogonal axis nodes (STAT3, FYN, MCL1) increase their activity through the compensatory signaling encoded in the model, recapitulating the de-repression mechanism described by Liaki et al. [1]. In PDAC, KRAS+EGFR inhibition triggers a pathway shift magnitude of 0.500 (50% increase in orthogonal axis activity

16

above untreated baseline), while the tri-axial combination constrains the shift to 0.400. Across cancers, MHS combinations showed a mean pathway shift of 0.490 compared to 0.434 for tri-axial combinations, indicating that same-axis targeting provokes stronger compensatory activation.

Interpretation and epistemic status. These simulation outputs are *deductive consequences* of the model's parameter structure, not independent empirical observations. The model encodes the tri-axial hypothesis through its axioms (elevated compensatory gains for orthogonal nodes, $g = 0.4$–0.7 vs. $g = 0.1$–0.2 for cascade nodes), and the tri-axial advantage follows logically from those axioms. The simulation therefore serves as a *hypothesis illustration*: it demonstrates what the Liaki tri-axial principle [1] quantitatively implies if compensatory signaling operates as assumed, and shows that MHS combinations that target topologically proximal same-axis nodes would leave orthogonal compensators intact under those assumptions. The simulation does not constitute evidence for the tri-axial hypothesis itself; independent validation would require fitting compensatory parameters from experimental time-course data (see Limitations).

Table 3: Systems biology simulation: intra-axial MHS vs. tri-axial combination therapy. ODE-based signaling models simulate adaptive pathway shifting under different treatment strategies. Time to resistance is measured as hours until tumor viability recovers above 0.5. Pathway shift magnitude measures compensatory orthogonal axis upregulation. All tri-axial combinations achieve lower final viability and greater resistance prevention.

Cancer	Strategy	Targets	Min V	Final V	AUC	TTR (d)	Shift
PDAC	Single (KRAS)	1	0.70	0.74	0.74	> 200	0.40
	Intra-axial MHS (KRAS+EGFR)	2	0.70	0.81	0.81	> 200	0.50
	Tri-axial (KRAS+CDK4+STAT3)	3	0.52	0.52	0.52	> 200	0.40
Melanoma	Single (BRAF)	1	0.63	0.63	0.64	> 200	0.50
	Intra-axial MHS (BRAF+MEK)	2	0.52	0.61	0.61	> 200	0.50
	Tri-axial (BRAF+CCND1+STAT3)	3	0.45	0.45	0.46	> 200	0.36
NSCLC	Single (EGFR)	1	0.57	1.00	1.00	> 200	0.40
	Intra-axial MHS (EGFR+KRAS)	2	0.57	0.67	0.67	> 200	0.40
	Tri-axial (KRAS+CCND1+MCL1)	3	0.43	0.57	0.57	> 200	0.52
CRC	Single (KRAS)	1	0.65	0.89	0.89	> 200	0.55
	Intra-axial MHS (KRAS+BRAF)	2	0.65	0.72	0.72	> 200	0.55
	Tri-axial (KRAS+CCND1+STAT3)	3	0.46	0.46	0.46	> 200	0.55
Breast	Single (CDK4)	1	0.63	0.77	0.77	> 200	0.43
	Intra-axial MHS (CDK4+CDK6)	2	0.61	0.65	0.65	> 200	0.50
	Tri-axial (CDK4+KRAS+STAT3)	3	0.36	0.36	0.37	> 200	0.33

Discussion

Biological significance

A consistent finding across cancer types is the convergent tri-axial architecture: STAT3 in the orthogonal position (78% of cancers), cell cycle regulators as downstream effectors, and cancer-specific oncogenes as upstream drivers. This convergence is biologically plausible—STAT3 is constitutively activated in >70% of solid tumors [2, 3] and sits downstream of multiple oncogenic drivers—but it also reflects an algorithmic confound: as a high-degree network hub, STAT3 is mathematically favored in any minimum-cost hitting set that optimizes coverage with the fewest genes. The conver-

gent *architecture* (orthogonal + downstream + upstream) extends the Liaki et al. [1] PDAC-specific tri-axial principle; whether STAT3 *specifically* occupies the orthogonal position in each cancer requires disease-specific validation.

STAT3 as orthogonal axis candidate: algorithmic selection, hub correction, and clinical evidence. STAT3 appears in 78% (60/77) of MHS predictions despite being rarely mutationally activated. Its selection is biologically coherent: STAT3 functions as a convergent survival node downstream of KRAS, EGFR, JAK, and SRC family kinases (including FYN), mediating immune evasion and stemness maintenance through BCL-XL, MCL-1, and stemness programs [8, 9, 58]. However, STAT3's high connectivity in signaling networks makes it a *mathematically optimal* hub for hitting-set coverage: it intersects many viability paths at low marginal cost. To address this algorithmic confound, we introduced a **proportional hub-gene penalty** in ranked triple scoring (Equation 3) that penalizes genes whose viability-path frequency exceeds the candidate median. This correction removed STAT3 from all 17 benchmarked cancer-type predictions and increased any-overlap recall from 34.9% (without hub penalty) to 37.2%, while producing predictions enriched for clinically validated targets (EGFR in 15/17, MET in 12/17 predictions). The hub penalty does not affect MHS predictions (which remain a static combinatorial optimization) but ensures that ranked triples better reflect cancer-specific biology rather than network topology.

CCND1 as a pan-cancer cell cycle vulnerability. The emergence of Cyclin D1 as the second most frequent MHS target (18 cancers, 23%) is novel. While CCND1 amplification is known in individual cancers, its role as a minimal hitting set component across cancer types has not been described. This suggests a pan-cancer cell cycle entry dependence potentially exploitable via CDK4/6 inhibitors. Notably, CDK4/6 inhibition can paradoxically *protect* hematopoietic stem cells from chemotherapy-induced damage by inducing reversible G1 arrest [59], suggesting potential for sequential or intermittent dosing strategies that reduce myelosuppression.

Static coverage vs. dynamic resistance. While 65% of cancers require only 2 targets for static viability path coverage, the Liaki PDAC results demonstrate that the third axis is essential for preventing adaptive resistance. Our ODE simulation, which encodes this hypothesis through its parameter structure (see Limitations), illustrates that under assumed compensatory cross-axis signaling the tri-axial advantage is ∼30% in viability terms, because same-axis targeting leaves orthogonal compensators intact. However, the magnitude of this advantage is a deductive consequence of the assigned compensatory gains and should not be treated as a quantitative prediction without experimental parameterization. The 2-target MHS represents a computational lower bound, the minimum for static coverage, but the Liaki et al. experimental evidence [1] argues that the number of targets for durable response should be guided by tri-axial coverage rather than the computational minimum.

Limitations

1. In silico predictions. All combinations are computational predictions requiring preclinical validation (cell lines, organoids, xenografts) before clinical translation.

2. Cell line representation. DepMap cell lines may not fully represent patient tumor heterogeneity. Some cancers have few lines (Ovarian Germ Cell Tumor, $n = 1$; Retinoblastoma, $n = 2$), increasing prediction variance. Several additional caveats apply: (i) *Cell line evolution*: even widely used cell lines (e.g., MCF-7) exhibit substantial genetic and transcriptional drift across laboratories; Ben-David et al. [60] showed that 27 MCF-7 strains from different laboratories displayed such divergent drug responses that 75% of compounds active in some strains were inactive in others. This means that DepMap essentiality scores are snapshots of specific passages and may not generalize across laboratories or to patient tumors. (ii) *Tumor microenvironment (TME)*: cell lines

18

lack stromal cells, immune infiltrate, vasculature, and extracellular matrix that critically modulate drug response in vivo. This is especially problematic for STAT3, which plays a dual immunological role: STAT3 promotes tumor-intrinsic survival but also drives immunosuppression by inhibiting dendritic cell maturation, T cell activation, and NK cell cytotoxicity [61, 62]. STAT3 inhibition in immune cells can paradoxically *enhance* anti-tumor immunity [62], meaning that the net effect of STAT3-targeting in vivo may differ substantially from cell-autonomous predictions. ALIN's entirely cell-autonomous predictions cannot capture these immune-mediated effects. (iii) *2D culture artifacts*: standard monolayer culture alters cell morphology, metabolism, and signaling relative to 3D spheroids or organoids; drug sensitivities measured in 2D may not predict 3D or in vivo responses.

3. Subtype heterogeneity. Pan-cancer-type analysis treats each OncoTree disease as homogeneous. Molecular subtypes (HER2+ vs. TNBC breast; EGFR-mutant vs. ALK+ NSCLC) have distinct dependencies, explaining benchmark misses for ERBB2 and ALK.

4. PDAC divergence. The pipeline predicts CCND1+KRAS as the minimal MHS for PDAC, while Liaki et al. [1] achieved complete regression with RAS + EGFR + STAT3. This divergence is instructive: the static hitting set covers all DepMap viability paths with 2 targets, but cannot capture the dynamic STAT3 activation via FYN that occurs upon dual-axis inhibition. Our ODE simulation (which encodes this compensatory mechanism through its parameter assumptions) is consistent with this divergence (PDAC MHS viability: 0.806 vs. tri-axial: 0.516 under stated assumptions), but this consistency is deductive rather than confirmatory since the model was designed to reproduce this pattern. For PDAC, a KRAS + CDK + STAT3 triple remains the most biologically grounded recommendation based on the Liaki et al. experimental evidence.

5. ODE simulation is illustrative, not evidential. The ODE model assigns elevated compensatory gains ($g = 0.4$–0.7) to orthogonal-axis nodes and lower gains ($g = 0.1$–0.2) to cascade nodes. This parameter structure *encodes* the assumption that orthogonal nodes upregulate when other axes are inhibited, meaning the tri-axial advantage is a *deductive consequence of the model's axioms*, not an independent prediction or empirical finding. The simulation demonstrates what the Liaki tri-axial hypothesis [1] quantitatively implies under these assumptions, but adds no evidential weight to the hypothesis itself. The sensitivity analysis (Supplementary Methods S5) confirms that the qualitative ordering (tri-axial < MHS < single < untreated) is preserved across $\pm 25\%$ parameter perturbations, including when compensatory gains are reduced to $g = 0.3$. This robustness analysis demonstrates that the tautology is stable under perturbation—not that the assumptions themselves are valid. None of the parameters (b_i, g_i, d_i, s_i) were fit to experimental data such as time-course phosphoproteomics, dose–response curves, or drug pharmacokinetics. Elevating this simulation from illustrative to predictive would require: (i) fitting compensatory gain parameters from time-course phosphoproteomics (e.g., STAT3 Tyr705 phosphorylation kinetics after MEK/EGFR inhibition); (ii) calibrating drug strength from dose–response data; (iii) validating the ODE dynamics against an independent cancer not used in parameter assignment. We identify this as a priority for future work and caution readers against treating the $\sim 30\%$ viability reduction as a quantitative prediction.

6. Druggability gaps. Several MHS components (CHMP4B, DNM2, HNRNPH1) lack clinical-stage drugs. However, 88% (68/77) of predictions include at least one druggable target.

7. Benchmark limitations. Against 43 independently curated multi-target gold-standard combinations spanning 25 cancer types, ALIN achieves 0.0% exact recall, 16.3% pair-overlap recall (7/43; $|G \cap T| \geq 2$), and 37.2% any-overlap recall (16/43; $|G \cap T| \geq 1$), leaving 27/43 combinations unrecovered. Cancer-level precision is 47.1% (8/17 evaluable cancer types), meaning that for nearly half of the cancer types where evaluation is possible, ALIN's predicted triple contains at least one validated target. Of the 27 misses, 18 are *structurally unmatchable*: 8 entries have cancer types

absent from the pipeline's DepMap coverage, and 13 entries include non-CRISPR targets (ESR1, CYP19A1, CYP17A1, KDR, PSMB5, HDAC6) that CRISPR knockout screens cannot capture (3 entries are both). On the 25 testable entries, ALIN achieves 60.0% any-overlap recall (15/25) and 28.0% pair-overlap recall (7/25), equalling or surpassing the driver-gene baseline (60.0% / 20.0%). Remaining misses reflect subtype-specific dependencies (BRAF V600E NSCLC, HER2+ breast), mutation-driven targets (FLT3), and dependencies accessible only through combinatorial CRISPR screens. ALIN's any-overlap recall (37.2% all / 60.0% testable) significantly exceeds the global-frequency baseline (11.6% / 12.0%; 3.2× improvement overall), demonstrating that cancer-specific scoring adds value beyond naïve gene popularity. At the pair-overlap level, ALIN (16.3% / 28.0%) matches or surpasses the driver-gene baseline (16.3% / 20.0%) and exceeds global-frequency (9.3% / 8.0%) and global random (9.8% / 14.3%). A candidate-pool random baseline—sampling 3 genes from the same per-cancer selective-essential pool that defines the pipeline's candidate set (median 1,269 genes)—achieves only 0.2% any-overlap recall (0.0% pair-overlap), confirming that the pipeline's scoring stages contribute virtually all observed performance; the DepMap pre-filtering step alone does not explain the results. The gold standard was constructed entirely from independent clinical sources (FDA approvals, Phase III trials) without reference to ALIN outputs [38, 39, 40, 42, 43, 44, 45, 46, 47, 48], mitigating the circularity risk of post-hoc curation. A formal ablation confirms no circularity: re-running the pipeline with the KNOWN_SYNERGIES lookup disabled (use_known_synergies=False) produces *identical* predictions for all 17 evaluable cancer types—recall, precision, and per-cancer triples are unchanged (see Limitation #16). Integrating expression, CNV, and subtype-specific data could improve recall.

8. STAT3 algorithmic bias and hub correction. STAT3's 78% frequency in MHS predictions is confounded by algorithmic hub preference: in any minimum-cost hitting-set formulation, high-degree nodes that intersect many viability paths at low marginal cost are mathematically favored [14]. STAT3, with its broad downstream convergence from KRAS, EGFR, JAK, and SRC-family kinases, is precisely such a hub. To address this, we implemented a **proportional hub-gene penalty** in the ranked triple scoring formula (Equation 3): for each candidate gene, the fraction of viability paths it appears in is computed; genes exceeding the median path frequency receive a penalty proportional to the excess (1.5× the excess above the median). This correction removed STAT3 from 100% of benchmarked cancer-type predictions (17/17), replacing it with cancer-specific oncogene targets (EGFR, MET, BRAF, KRAS) and improving any-overlap benchmark recall from 34.9% to 37.2%. The hub penalty does not affect MHS predictions (which retain STAT3 at 78%) but ensures that clinically actionable ranked triples are not dominated by a single high-connectivity node. STAT3-directed agents have shown limited single-agent clinical efficacy [4, 5], although STAT3 may remain relevant as a combination partner in specific biomarker-selected contexts (pSTAT3 Tyr705-positive tumors [5]; PROTAC-based approaches [13]).

9. Parameter calibration. Several pipeline parameters were initially introduced as fixed design choices. We implemented a systematic parameter tuning framework (parameter_tuning.py) to calibrate these against external references. (i) *Threshold sensitivity*: a sweep of 500 configurations revealed that candidate pool size varies ∼23-fold (191–4,429 genes) across tested ranges of $\tau_{\text{dep}} \in [-0.3, -0.7]$, $\theta \in [0.15, 0.40]$, and pan-essential cutoff $\in [0.80, 0.95]$, with the dependency threshold exerting the largest influence. The current defaults ($\tau_{\text{dep}} = -0.5$, $\theta = 0.30$, pan-essential $= 0.90$) produce moderate-sized candidate pools; we now report the full sensitivity surface so users can assess the effect of alternative choices. (ii) *Cluster-count calibration*: we evaluated the clustering heuristic against curated KEGG/Reactome pathway annotations (8 pathways, 5 cancer types). NMI increased from 0.41 (k=5) to 0.71 (k=50), with the default k=15 achieving NMI=0.58. This provides quantitative justification for the current default while identifying that higher k values improve pathway-annotation alignment at the cost of module granularity. (iii) *Scoring weights*: the

combination-score weights (0.22/0.18/0.18/0.18/0.14/0.10) were subjected to local $\pm 20\%$ perturbation analysis; a grid search over 7 structured weight presets is implemented for cross-validated optimization against the gold-standard benchmark. (iv) *Full grid search*: a two-stage grid-search tuner (upstream parameters fixed with original weights, then weights optimized with best upstream parameters) is available via `--tune-parameters --tune-mode grid`, enabling end-to-end hyperparameter optimization against the 43-entry gold standard. While the current defaults remain reasonable design choices supported by community practice [18, 24], the tuning infrastructure enables formal calibration as larger gold-standard datasets become available.

10. LOCO evaluation is not true cross-validation. The leave-one-cancer-out (LOCO) partitioned evaluation reports per-cancer recall by partitioning the gold standard and evaluating the *same* pipeline predictions on each partition. Critically, the pipeline is *not* re-run with the held-out cancer's DepMap data excluded; the predictions for every cancer type are generated from a single full-data pipeline run. This means that LOCO evaluation tests whether predictions happen to match held-out gold-standard entries—a useful consistency check—but does *not* test generalization to genuinely unseen cancer types. True held-out cross-validation would require, at each fold, re-running the entire pipeline (DepMap filtering → viability-path inference → MHS → triple scoring) with the held-out cancer's cell lines excluded from the dependency matrix. This is computationally expensive (each fold re-runs the full pipeline for ~ 76 cancers) and is flagged as a priority for future work. Until true held-out CV is implemented, the LOCO partitioned evaluation results (exact recall $12.5\% \pm 33.1\%$) should be interpreted as lower bounds on in-sample consistency, not as evidence of generalization.

11. MHS solver is primarily greedy for typical candidate pools. The weighted hitting-set problem is NP-hard, and typical candidate pools contain hundreds of genes (~ 200–4,400 depending on thresholds). The implementation employs a solver hierarchy: (i) greedy weighted set cover ($\ln n$-approximation; always run); (ii) ILP via `scipy.optimize.milp` for pools ≤ 500 genes (provably optimal subject to a 30-second timeout); (iii) exhaustive enumeration for pools ≤ 20 genes. For the majority of cancer types the ILP solver provides provably optimal solutions; however, for cancers with very large candidate pools (>500 genes) the greedy approximation may be the only feasible solver. Each solution is annotated with the solver that produced it. Earlier versions of this paper described exhaustive enumeration for pools ≤ 25 genes, a threshold that was effectively never reached in practice; the current implementation replaces this with the ILP solver, which handles realistic pool sizes.

12. Perturbation data is curated, not systematic. The perturbation-response module (Method 5) comprises manually curated summaries from ~ 15 published kinase-inhibitor studies encoded as Python dictionaries, not systematic high-throughput perturbation profiling. This stands in stark contrast to genome-scale resources such as LINCS L1000 [33] (>1.3 million gene-expression profiles across thousands of perturbagens and multiple cell lines) or the Connectivity Map [34] ($\sim 7,000$ expression profiles). Key concerns: (i) *Coverage*: only 13 unique target signatures (KRAS, EGFR, BRAF, MEK1, CDK4, PIK3CA, MTOR, SRC, STAT3, BCL2, JAK1, MET, ALK) plus 5 isoform aliases are curated, versus $>20,000$ perturbagens in L1000—a $\sim 1,500\times$ scale gap. (ii) *Biologically dubious aliases*: several aliases share identical perturbation profiles despite distinct substrate specificities (FYN→SRC, CDK6→CDK4, JAK2→JAK1, MAP2K1/MAP2K2→MEK1). FYN and SRC, for example, are both Src-family kinases but phosphorylate overlapping-yet-distinct substrates; treating their perturbation responses as identical is a simplification that could misdirect resistance predictions. (iii) *Arbitrary confidence scores*: the confidence values (0.85–0.95) assigned to each signature are author-set heuristics reflecting perceived study quality, not formal statistical measures. (iv) *Knowledge bias in* β_{pert}: the perturbation bonus rewards combinations concordant with this curated expert knowledge, meaning that well-studied kinases with extensive published

inhibitor data disproportionately benefit from the scoring, while under-studied targets receive no perturbation bonus regardless of their biological importance. Integration with LINCS L1000 or CMap would replace curated dictionaries with data-driven genome-wide perturbation signatures, eliminating the need for aliases and arbitrary confidence scores; this is flagged as a priority for future work.

13. Viability paths lack formal biological validation. Viability paths are inferred by four computational methods (co-essentiality clustering, signaling topology, cancer-specific testing, perturbation response) but are *not* validated against external pathway databases via formal enrichment analysis. Specifically: (i) *No pathway enrichment testing*: individual viability paths are never tested for over-representation in KEGG, Reactome, or Gene Ontology pathways using hypergeometric or GSEA methods. The NMI calibration (0.58 at k=15) evaluates co-essentiality *clusters* against 8 hardcoded pathway gene sets, but only 9–18 annotated genes per cancer type overlap with the reference sets—far too few for statistically meaningful inference. (ii) *No statistical testing for Methods 1–3*: co-essentiality modules are formed by a threshold-based heuristic (Jaccard + Ward's linkage + $n/5$ cut) with no hypothesis test assessing whether the resulting modules are more biologically coherent than random gene groups; signaling paths are selected by a hard pruning threshold ($S_{\text{path}} \geq 0.3$), not by enrichment significance; perturbation paths are curated (see Limitation #12). Only Method 4 (cancer-specific dependencies) employs formal statistical testing with FDR correction. (iii) *Inflated path counts*: viability path counts (4–103 per cancer) are partly inflated by a "consensus path" containing all selective genes—a superset path that any single selective gene trivially intersects—and by exhaustive signaling-path enumeration from the OmniPath network. The wide range (4–103) partly reflects the number of signaling edges in OmniPath for well-studied cancers rather than genuinely distinct survival mechanisms. (iv) *Tautological coverage*: "100% viability path coverage" is a mathematical guarantee of the MHS solver, which is defined to find a set intersecting every inferred path; it does not mean that every biological survival mechanism has been blocked. The solver covers all of its own inferred paths, which is trivially achievable when the solver's objective function is coverage maximization. A hypergeometric ORA module (`parameter_tuning.py --mode enrich`) testing each viability path against 12 canonical pathway gene sets is implemented but should be extended to genome-wide pathway databases (MSigDB, Reactome API) for comprehensive validation.

14. CRISPR knockout $\neq$ pharmacological inhibition (partially mitigated). ALIN's predictions are derived from CRISPR-Cas9 loss-of-function screens (DepMap), which achieve complete, irreversible gene ablation. Pharmacological inhibition is fundamentally different: drugs produce partial, reversible, dose-dependent target modulation with off-target effects, pharmacokinetic limitations, and resistance mechanisms (efflux pumps, target mutations, metabolic inactivation) absent from genetic screens. Lin et al. [50] demonstrated that CRISPR knockout of MELK—a putative cancer dependency targeted in clinical trials—had no effect on cancer cell fitness, while the MELK inhibitor OTS167 still killed cells through off-target mechanisms, illustrating that genetic and pharmacological perturbations can yield opposite conclusions about target essentiality. More broadly, Gonçalves et al. [51] integrated pharmacological and CRISPR screens across 484 cell lines and found that only ∼25% of drugs' killing patterns were phenocopied by CRISPR knockout of their nominal targets. To partially address this gap, we implemented a *CRISPR–drug concordance filter* (`pharmacological_validation.py`) that cross-validates each predicted target against PRISM drug sensitivity data in matched cell lines: targets where CRISPR essentiality does not correlate with drug-induced killing are flagged as potentially discordant. An *evidence tier system* further classifies each cancer's predictions by the level of pharmacological support available (Tier 1–4; see Methods). These mitigations reduce but do not eliminate the CRISPR–drug gap: concordance analysis requires drugs targeting the predicted gene to exist in the PRISM screen, and many novel

targets (CHMP4B, DNM2) lack pharmacological agents entirely.

15. Single-gene-to-combination inference gap (partially mitigated, new co-essentiality estimator). ALIN infers combination targets from single-gene CRISPR knockout data, but genetic interactions are non-additive: the effect of simultaneously perturbing two genes cannot be reliably predicted from their individual perturbation effects. Norman et al. [52] used Perturb-seq (combinatorial CRISPR with single-cell transcriptomic readout) to show that dual-gene perturbations frequently produce transcriptional programs absent from either single perturbation, including epistatic and synergistic interactions that are invisible to single-gene screens. Shen et al. [53] systematically mapped ∼142,000 pairwise genetic interactions via combinatorial CRISPR-Cas9 screens and found that genetic interaction patterns predicted combinatorial drug responses at approximately 75% precision—useful but far from deterministic. To partially mitigate this limitation, we replaced the original heuristic synergy score (13 curated pairs + pathway diversity) with a *co-essentiality-based interaction estimator* (`pharmacological_validation.py`) that computes Jaccard similarity between genes' DepMap dependency profiles: low co-essentiality (genes essential in different cell lines) indicates independent pathway requirements and higher synergy potential, while high co-essentiality indicates redundancy. The data-driven score blends co-essentiality (60%) with pathway diversity (40%), grounding synergy estimation in empirical data rather than expert curation. Nevertheless, co-essentiality cannot capture emergent genetic interactions (buffering, synthetic lethality, or resistance mechanisms) that arise only upon simultaneous perturbation. Combinatorial CRISPR screens or high-throughput drug-combination assays remain necessary to validate predicted triples.

16. KNOWN_SYNERGIES ablation (no circularity). The synergy scoring stage originally included a `KNOWN_SYNERGIES` dictionary that hardcoded synergy scores for 13 gene pairs (e.g., BRAF+MAP2K1=0.95, EGFR+MET=0.85) overlapping with gold-standard combinations, raising a circularity concern: could the pipeline's benchmark performance be inflated by baked-in knowledge of the evaluation targets? To test this, we added a `use_known_synergies` parameter and re-ran the full pipeline for all 17 evaluable cancer types with the curated synergy lookup disabled. Without `KNOWN_SYNERGIES`, synergy is computed purely from pathway diversity (fraction of distinct pathway modules covered by the triple's targets) and co-essentiality interaction estimation. The ablation result is unambiguous: **all recall and precision metrics are identical** with and without the curated synergy lookup—0% exact, 7.0% superset, 16.3% pair-overlap, 37.2% any-overlap recall, and 47.1% precision (58.3% testable precision). Every one of the 17 evaluable cancer types selects the same best triple. This demonstrates that `KNOWN_SYNERGIES` affects the internal synergy score magnitude but does not change which triple is ranked first, because pathway diversity and co-essentiality already discriminate between candidate triples sufficiently. The curated pairs are therefore redundant for ranking and introduce no circularity into benchmark evaluation. We retain the `use_known_synergies=True` default for backward compatibility but recommend the ablated mode (`--no-known-synergies`) for any future benchmark comparisons.

Comparison to existing approaches

Our minimal hitting set formulation differs from existing combination prediction methods: (1) **Empirical screens** (e.g., drug synergy matrices) are expensive and limited to available drugs; we predict target-level combinations that can be mapped to multiple drugs. (2) **Network-based methods** (e.g., shortest paths between driver and effector) do not guarantee path coverage; our hitting set formulation does. (3) **Machine learning approaches** often lack interpretability; our cost function explicitly encodes toxicity, specificity, and druggability. (4) **Fixed-size approaches** (pairs only, or triples only) impose combination size without biological justification; our approach discovers the computational minimum via MHS optimization and then generates pathway-diverse

triples guided by the tri-axial principle. The 37.2% any-overlap recall against 43 independently curated gold-standard combinations (60.0% on the 25 testable entries), 3.2× the global-frequency baseline (11.6%) and above global random (21.9%; $p < 0.001$), with 47.1% cancer-level precision (58.3% testable), provides evidence of non-random target recovery while identifying substantial areas for improvement. A candidate-pool random baseline sampling from the same per-cancer selective-essential gene pool the pipeline uses achieves only 0.2% any-overlap recall, confirming that the scoring and ranking stages—not merely the DepMap pre-filtering step—are responsible for ALIN's performance. At pair-overlap level ($|G \cap T| \geq 2$), ALIN achieves 16.3% overall (28.0% testable), matching or surpassing the driver-gene baseline (16.3% / 20.0%). The driver-gene baseline's any-overlap recall (44.2% overall, 60.0% testable) ties ALIN on testable entries, highlighting that curated clinical knowledge remains a strong comparator and motivating integration of expression, CNV, and subtype data.

Future Work

Phase 1: Suggested preclinical experiments

- **Tri-axial combination testing in cell lines**: STAT3's computational frequency motivates testing whether STAT3 inhibition enhances existing targeted therapy combinations in cell-based assays. Initial experiments could test STAT3 degraders (e.g., PROTACs [13]) alongside CDK4/6 inhibitors in breast cancer lines, or alongside BRAF/MEK inhibitors in melanoma lines, in pSTAT3 Tyr705-positive contexts. These are *preclinical hypotheses* requiring standard drug-combination synergy assays (e.g., Bliss independence or Loewe additivity), *not* clinical trial proposals. CRISPR knockout does not recapitulate pharmacological inhibition [50, 51], so cell-line viability assays with actual drugs are an essential first validation step.

- **Priority preclinical combinations for cell-line testing**: (1) Melanoma: BRAF inhibitor + CDK4/6 inhibitor + STAT3 degrader; (2) Ewing Sarcoma: CDK4/6 inhibitor + STAT3 degrader (FLI1 remains undruggable); (3) PDAC: KRAS inhibitor + CDK4/6 inhibitor + STAT3 degrader (critical comparison of MHS vs. tri-axial combination); (4) NSCLC: CDK inhibitor + MCL1 inhibitor (where MCL1 replaces STAT3 as orthogonal axis). Combination-index analysis and long-term clonogenic assays would assess synergy and durability respectively. Interpretation must account for cell-line evolution artifacts [60] and the absence of tumor microenvironment context.

- **Validation considerations**: Drug combination assays (e.g., 6×6 dose matrices with Bliss independence scoring) should compare triple vs. best dual to quantify the contribution of the third axis. Long-term resistance cultures (8–12 weeks) could assess durability, but results in 2D culture have limited predictive value for in vivo responses [60]. Organoid models and patient-derived xenografts would provide more physiologically relevant validation contexts.

Methodological improvements

- **Subtype-specific analysis**: Splitting by molecular subtype (HER2+/TNBC breast; EGFR-mutant/ALK+/KRAS+ NSCLC) should address benchmark misses for ERBB2, BRAF V600E, and MET-amplified subtypes. Integrating CCLE expression and CNV data could improve recall from 37.2% (60.0% testable) and precision from 47.1% (58.3% testable), further separating ALIN from the driver-gene baseline on testable entries.

- **Dynamic pathway modeling**: Extending the ODE simulation to all 77 cancers and incorporating patient-derived phosphoproteomics time-course data for parameter estimation. Agent-based models could capture intratumoral heterogeneity and clonal selection dynamics.

- **Expanded gold standard**: The current 43-entry gold standard spans 25 cancer types; expansion to 60+ entries with KRAS G12D inhibitors (MRTX1133), recent immunotherapy combinations, and emerging Phase III data [17, 63] would provide a more stringent benchmark.

- **Viability path biological validation**: Systematic hypergeometric over-representation analysis (ORA) or GSEA of each inferred viability path against genome-wide pathway databases (MSigDB Hallmark + C2 curated, Reactome API, GO Biological Process) would establish what fraction of inferred paths correspond to known biological pathways and identify paths that may represent statistical noise. A preliminary ORA module is implemented (`parameter_tuning.py --mode enrich`) but currently tested against only 12 curated pathway gene sets; extension to genome-wide databases is a priority.

- **Druggability**: Indirect targeting strategies for undruggable MHS components (CHMP4B, DNM2, HNRNPH1) via synthetic lethality.

Note on STAT3 inhibitors: While STAT3 remains in 78% of MHS predictions, the hub-gene penalty removes it from all ranked triple predictions for the 17 benchmarked cancer types. The disconnect between STAT3's computational importance in MHS and its clinical track record is informative: napabucasin failed its Phase 3 primary endpoint in unselected refractory CRC [5], and other small-molecule STAT3 inhibitors have generally shown limited single-agent efficacy in solid tumors [4]. Three considerations remain relevant: (1) the Liaki et al. [1] PDAC success used SD-36, a STAT3 PROTAC [13] that degrades the protein rather than inhibiting its catalytic activity; (2) napabucasin showed significant benefit specifically in pSTAT3-positive patients (HR 0.41, $p = 0.0025$) [5]; (3) STAT3's role may be most critical in *combination* (tri-axial blockade) rather than as monotherapy. The hub penalty addresses the algorithmic confound while retaining STAT3 as a candidate in MHS where its mathematical properties are appropriate.

Conclusion

ALIN Framework applies the tri-axial inhibition principle—simultaneously targeting downstream, upstream, and orthogonal signaling axes—from Liaki et al.'s experimentally validated PDAC system [1] to 77 cancer types *computationally*. Whether this principle genuinely extends beyond PDAC is an open experimental question; ALIN generates testable hypotheses, not validated therapeutic regimens.

The central computational finding is architectural convergence: STAT3 occupies the orthogonal position in 78% of MHS predictions, cell cycle regulators serve as downstream effectors, and cancer-specific oncogenes provide the upstream signal. A hub-gene penalty in the ranked triple scoring stage corrects STAT3's algorithmic over-representation, producing cancer-specific predictions enriched for validated targets (EGFR in 15/17, MET in 12/17 benchmarked cancers). This corrected architecture retains the tri-axial principle while yielding clinically plausible predictions. Critically, CRISPR-based essentiality (complete gene knockout) does not equate to pharmacological inhibition (partial, reversible, off-target-prone) [50, 51], and single-gene DepMap screens cannot capture the emergent genetic interactions that govern combination responses [52, 53]. Our ODE

simulation illustrates that, under the model's assumed compensatory signaling structure (parameters assigned by biological role, not fit to data; see Limitations), tri-axial combinations yield ~30% lower tumor viability than same-axis combinations across five cancers. This illustrative result is a deductive consequence of the model's axioms rather than an independent quantitative prediction; experimental parameterization from phosphoproteomics time-course data is required to determine whether the actual magnitude of tri-axial advantage matches these assumptions.

Benchmarking achieves 37.2% any-overlap recall and 16.3% pair-overlap recall against 43 independently curated multi-target gold-standard combinations spanning 25 cancer types (60.0% and 28.0% on the 25 testable entries; $3.2\times$ the 11.6% global-frequency baseline; $p < 0.001$ vs. random). A candidate-pool random baseline sampling from the per-cancer selective-essential gene pool achieves only 0.2% any-overlap, confirming that the scoring stages—not merely DepMap prefiltering—drive performance. Cancer-level precision is 47.1% (8/17 evaluable cancers; 58.3% on 12 testable cancers), confirming that a substantial fraction of ALIN's cancer-type predictions contain independently validated targets (Table 2). On testable entries, ALIN equals the driver-gene baseline at any-overlap (60.0%) and surpasses it at pair-overlap (28.0% vs. 20.0%), indicating that the pipeline's advantage is clearest when the gold standard is restricted to entries compatible with CRISPR/DepMap data. While exact-combination recall remains at 0%, 88% of predictions include druggable targets. These predictions are hypotheses for preclinical testing—not clinical recommendations. Multi-step experimental validation (cell-line synergy assays, organoid models, xenograft studies) is required before any translation; the gap between CRISPR essentiality data and pharmacological reality (Limitation #14) and between single-gene knockouts and combination responses (Limitation #15) demands particular caution in interpreting computational target predictions as therapeutic proposals.

Data and code availability

Data: DepMap (`https://depmap.org`), PRISM (`https://depmap.org/repurposing`), OmniPath (`https://omnipathdb.org`), STRING [37] (`https://string-db.org`). Code: `https://github.com/royerz2/Pan-Cancer-X-Node-Target-Discovery-System` with `run_full_pipeline.sh` for full reproducibility. Archived at Zenodo (DOI: 10.5281/zenodo.18517646). Detailed mathematical derivations and parameter justifications are provided in the Supplementary Methods document. See DATA_AVAILABILITY.md for file URLs and licenses.

Competing interests

The author declares no competing interests.

Author contributions (CRediT)

Roy Erzurumluoğlu: Conceptualization, Methodology, Software, Validation, Formal Analysis, Investigation, Data Curation, Writing – Original Draft, Writing – Review & Editing, Visualization.

Acknowledgements

Bibliography

References

[1] V. Liaki, S. Barrambana, M. Kostopoulou, C. G. Lechuga, et al. A targeted combination therapy achieves effective pancreatic cancer regression and prevents tumor resistance. *bioRxiv*, 2025. Preprint.

[2] H. Yu and R. Jove. The STATs of cancer—new molecular targets come of age. *Nature Reviews Cancer*, 4(2):97–105, 2004. PMID:14964307.

[3] D. A. Frank. STAT3 as a central mediator of neoplastic cellular transformation. *Cancer Letters*, 251(2):199–210, 2007. PMID:17129668.

[4] D. E. Johnson, R. A. O'Keefe, and J. R. Grandis. Targeting the IL-6/JAK/STAT3 signalling axis in cancer. *Nature Reviews Clinical Oncology*, 15:234–248, 2018. PMID:29405201.

[5] D. J. Jonker, L. Nott, T. Yoshino, et al. Napabucasin versus placebo in refractory advanced colorectal cancer: a randomised phase 3 trial. *The Lancet Gastroenterology & Hepatology*, 3(4):263–270, 2018.

[6] J. S. Bergholz and J. J. Zhao. How compensatory mechanisms and adaptive rewiring have shaped our understanding of therapeutic resistance in cancer. *Cancer Research*, 81(24):6074–6077, 2021.

[7] Y. Xin, H. Zhang, Y. Li, et al. Drug resistance mechanisms in cancers: Execution of pro-survival strategies. *Acta Pharmaceutica Sinica B*, 14(7):2943–2960, 2024.

[8] R. A. Chougule, J. U. Kazi, and L. Rönnstrand. FYN expression potentiates FLT3-ITD induced STAT5 signaling in acute myeloid leukemia. *Oncotarget*, 7(9):9964–9974, 2016.

[9] Y. K. Choi, B. I. Yoon, Y. S. Won, et al. Stat3 mediates fyn kinase driven dopaminergic differentiation and promotes neuroprotection in cellular models of Parkinson's disease. *bioRxiv*, 2024. Preprint.

[10] Z. Ma, Y. Peng, Y. Gong, et al. Highlight on a phase III clinical candidate daraxonrasib (RMC-6236): Discovery, optimization, and biological evaluation. *Journal of Medicinal Chemistry*, 68(12):10167–10183, 2025.

[11] N. Ioannou, A. G. Dalgleish, A. M. Seddon, et al. Anti-tumour activity of afatinib, an irreversible ErbB family blocker, in human pancreatic tumour cells. *British Journal of Cancer*, 105(10):1554–1562, 2011.

[12] F. Huguet, M. Fernet, N. Giocanti, V. Favaudon, and A. K. Larsen. Afatinib, an irreversible EGFR family inhibitor, shows activity toward pancreatic cancer cells, alone and in combination with radiotherapy, independent of KRAS status. *Targeted Oncology*, 11(3):371–381, 2016.

[13] L. Bai, H. Zhou, R. Xu, et al. Structure-based discovery of SD-36 as a potent, selective, and efficacious PROTAC degrader of STAT3 protein. *Journal of Medicinal Chemistry*, 62(15):6774–6789, 2019.

[14] P. Vera-Licona, E. Bonnet, E. Barillot, and A. Zinovyev. OCSANA: optimal combinations of interventions from network analysis. *Bioinformatics*, 29(12):1571–1573, 2013.

[15] Y. Murakami, L. P. Tripathi, P. Prathipati, and K. Mizuguchi. Network analysis and in silico prediction of protein-protein interactions with applications in drug discovery. *Current Opinion in Structural Biology*, 44:134–142, 2017.

[16] H. Julkunen, A. Cichonska, M. Srivastava, S. Alemany, S. Kaski, and J. Rousu. Modeling drug combination effects via latent tensor reconstruction. *Bioinformatics*, 39(Supplement_1):i43–i51, 2023. PMC:10022091.

[17] M. P. Menden, D. Wang, M. J. Mason, et al. Community assessment to advance computational prediction of cancer drug combinations in a pharmacogenomic screen. *Nature Communications*, 10:2674, 2019. DREAM Challenge. PMID:31380352.

[18] J. M. Dempster, I. Boyle, F. Vazquez, et al. Chronos: a cell population dynamics model of CRISPR experiments that improves inference of gene fitness effects. *Genome Biology*, 22:343, 2021.

[19] A. Tsherniak, F. Vazquez, P. G. Montgomery, et al. Defining a cancer dependency map. *Cell*, 170(3):564–576, 2017.

[20] D. Türei, A. Valdeolivas, L. Gul, et al. OmniPath: integrated knowledgebase for multi-omics analysis. *Nucleic Acids Research*, 54(D1):D652–D662, 2026.

[21] S. M. Corsello, R. T. Nagari, R. D. Spangler, J. Rossen, M. Kocak, J. G. Bryan, et al. Discovering the anticancer potential of non-oncology drugs by systematic viability profiling. *Nature Cancer*, 1:235–248, 2020.

[22] W. Yang, J. Soares, P. Greninger, et al. Genomics of drug sensitivity in cancer (GDSC): a resource for therapeutic biomarker discovery in cancer cells. *Nucleic Acids Research*, 41(D1):D955–D961, 2013.

[23] F. Iorio, T. A. Knijnenburg, D. J. Vis, et al. A landscape of pharmacogenomic interactions in cancer. *Cell*, 166(3):740–754, 2016.

[24] F. M. Behan, F. Iorio, G. Picco, et al. Prioritization of cancer therapeutic targets using CRISPR-Cas9 screens. *Nature*, 568(7753):511–516, 2019.

[25] K. Shimada, J. A. Bachman, J. L. Muhlich, et al. shinydepmap, a tool to identify targetable cancer genes and their functional connections from cancer dependency map data. *eLife*, 10:e57116, 2021.

[26] Robin M. Meyers, Jordan G. Bryan, James M. McFarland, Barbara A. Weir, Ann E. Sizemore, Han Xu, Neekesh V. Dharia, Philip G. Montgomery, Glenn S. Cowley, Sasha Pantel, et al. Computational correction of copy number effect improves specificity of CRISPR-Cas9 essentiality screens in cancer cells. *Nature Genetics*, 49(12):1779–1784, 2017. PMID:29083409.

[27] Clare Pacini, Joshua M. Dempster, Isabella Boyle, Emanuel Gonçalves, Hanna Najgebauer, Emre Karakoc, Dennis van der Meer, Andrew Barthorpe, Howard Lightfoot, Patricia Jaaks, et al. Integrated cross-study datasets of genetic dependencies in cancer. *Nature Communications*, 12:1661, 2021. PMID:33712601.

[28] E. Eisenberg and E. Y. Levanon. Human housekeeping genes, revisited. *Trends in Genetics*, 29(10):569–574, 2013.

[29] B. W. Hounkpe, F. Chenou, F. de Lima, and E. V. De Paula. HRT Atlas v1.0 database: redefining human and mouse housekeeping genes and candidate reference transcripts by mining massive RNA-seq datasets. *Nucleic Acids Research*, 49(D1):D947–D955, 2021.

[30] J. Pan, R. M. Meyers, B. C. Michel, et al. Interrogation of mammalian protein complex structure, function, and membership using genome-scale fitness screens. *Cell Systems*, 6(5):555–568, 2018.

[31] Yoav Benjamini and Yosef Hochberg. Controlling the false discovery rate: A practical and powerful approach to multiple testing. *Journal of the Royal Statistical Society: Series B (Methodological)*, 57(1):289–300, 1995.

[32] J. Cohen. *Statistical Power Analysis for the Behavioral Sciences*. Lawrence Erlbaum Associates, 2nd edition, 1988.

[33] Aravind Subramanian, Rajiv Narayan, Steven M. Corsello, David D. Peck, Ted E. Natoli, Xiaodong Lu, Joshua Gould, John F. Davis, Andrew A. Tubelli, Jacob K. Asiedu, David L. Lahr, Jodi E. Hirschman, Zihan Liu, Melanie Donahue, Bina Julian, Musrat Khan, David Wadden, Ian C. Smith, Daniel Lam, Arthur Liberzon, Courtney Tong, Marielle Moore, Stephanie Hilber, Mismisut Chetah, Elizabeth A. Gates, Courtney Korber, Justin Shih, Sara E. Harding, Maria Vrcic, and Todd R. Golub. A next generation connectivity map: L1000 platform and the first 1,000,000 profiles. *Cell*, 171(6):1437–1452.e17, 2017. PMID:29195078.

[34] Justin Lamb, Emily D. Crawford, David Peck, Joshua W. Modell, Irene C. Blat, Matthew J. Wrobel, Jim Lerner, Jean-Philippe Brunet, Aravind Subramanian, Kenneth N. Ross, Michael Reich, Haley Hieronymus, Guo Wei, Scott A. Armstrong, Stephen J. Haggarty, Paul A. Clemons, Ru Wei, Steven A. Carr, Eric S. Lander, and Todd R. Golub. The connectivity map: Using gene-expression signatures to connect small molecules, genes, and disease. *Science*, 313(5795):1929–1935, 2006. PMID:17008526.

[35] Kristina Preuer, Richard P. I. Lewis, Sepp Hochreiter, Andreas Bender, Krishna C. Bulusu, and Günter Klambauer. DeepSynergy: predicting anti-cancer drug synergy with deep learning. *Bioinformatics*, 34(9):1538–1546, 2018. PMID:29253077.

[36] Patricia Jaaks, Elizabeth A. Coker, Daniel J. Vis, Olivia Edwards, Emily F. Carpenter, Simonetta M. Leto, Lisa Dwane, Rizwan Sasber, Mark Golber, Samixa Lamba, et al. Effective drug combinations in breast, colon and pancreatic cancer cells. *Nature*, 603(7903):166–173, 2022. PMID:35197630.

[37] D. Szklarczyk, R. Kirsch, M. Koutrouli, et al. String database in 2025: protein networks with directionality, expanded organism coverage, and new evidence channels. *Nucleic Acids Research*, 53(D1):D730–D738, 2025.

[38] G. V. Long, D. Stroyakovskiy, H. Gogas, et al. Combined BRAF and MEK inhibition versus BRAF inhibition alone in melanoma. *New England Journal of Medicine*, 371(20):1877–1888, 2014.

[39] D. Planchard, B. Besse, H. J. Groen, et al. Dabrafenib plus trametinib in patients with previously treated BRAF V600E-mutant metastatic non-small cell lung cancer. *The Lancet Oncology*, 17(7):984–993, 2016. PMID:27283860.

[40] S. Kopetz, A. Grothey, R. Yaeger, et al. Encorafenib, binimetinib, and cetuximab in BRAF V600E-mutated colorectal cancer. *New England Journal of Medicine*, 381(17):1632–1643, 2019. PMID:31566309.

[41] J. Larkin, P. A. Ascierto, B. Dréno, et al. Combined vemurafenib and cobimetinib in BRAF-mutated melanoma. *New England Journal of Medicine*, 371(20):1867–1876, 2014. PMID:25105994.

[42] K. Park, E. B. Haura, N. B. Leighl, et al. Amivantamab in EGFR exon 20 insertion-mutated non-small-cell lung cancer. *Journal of Clinical Oncology*, 39(30):3391–3402, 2021. PMID:34043995.

[43] L. V. Sequist, J. Y. Han, M. J. Ahn, et al. Osimertinib plus savolitinib in patients with EGFR mutation-positive, MET-amplified, non-small-cell lung cancer after progression on EGFR tyrosine kinase inhibitors. *The Lancet Oncology*, 21(3):373–386, 2020. PMID:32234522.

[44] J. Baselga, I. Bradbury, H. Eidtmann, et al. Lapatinib with trastuzumab for HER2-positive early breast cancer (NeoALTTO). *The Lancet*, 379(9816):633–640, 2012. PMID:22153890.

[45] N. C. Turner, J. Ro, F. André, et al. Palbociclib in hormone-receptor-positive advanced breast cancer. *New England Journal of Medicine*, 373(3):209–219, 2015. PMID:26394241.

[46] R. J. Motzer, T. E. Hutson, H. Glen, et al. Lenvatinib, everolimus, and the combination in patients with metastatic renal cell carcinoma. *The Lancet Oncology*, 16(15):1473–1482, 2015. PMID:26116099.

[47] N. Daver, A. E. Perl, J. Maly, et al. Venetoclax plus gilteritinib for FLT3-mutated relapsed/refractory acute myeloid leukemia. *Journal of Clinical Oncology*, 40(35):4048–4059, 2022. PMID:35443125.

[48] E. Ciruelos, P. Villagrasa, T. Pascual, et al. Palbociclib and trastuzumab in HER2-positive advanced breast cancer: results from the phase III PATINA trial. *Journal of Clinical Oncology*, 2024. PMID:36631847.

[49] V. Bhardwaj, Y. Zhan, M. A. Cortez, et al. MET inhibitor ficlatuzumab combined with cetuximab in head and neck squamous cell carcinoma. *Cancer Letters*, 2019. PMID:32416071.

[50] Ann Lin, Christopher J. Giuliano, Annabelle Palladino, Kristen M. John, Christine Abramowicz, Monet Lou Yuan, Edward L. Sausville, Devon A. Lukow, Luwei Liu, Alexander R. Chait, Zachary C. Galluzzo, Craig Tucker, Vishal Bhatt, Jessie Hu, and Jason M. Sheltzer. CRISPR/Cas9 mutagenesis invalidates a putative cancer dependency targeted in on-going clinical trials. *eLife*, 6:e24179, 2017.

[51] Emanuel Gonçalves, Aldo Segura-Cabrera, Clare Pacini, Gabriele Picco, Fiona M. Behan, Patricia Jaaks, Elizabeth A. Coker, Donny van der Meer, Andrew Barthorpe, Howard Lightfoot, Tatiana Mironenko, Alexandra Beck, Laura Richardson, Wanjuan Yang, Frank B. Garnari, Francesco Iorio, and Mathew J. Garnett. Drug mechanism-of-action discovery through the integration of pharmacological and CRISPR screens. *Molecular Systems Biology*, 16(7):e9405, 2020.

[52] Thomas M. Norman, Max A. Horlbeck, Joseph M. Replogle, Alex Y. Ge, Albert Xu, Marco Jost, Luke A. Gilbert, and Jonathan S. Weissman. Exploring genetic interaction manifolds constructed from rich single-cell phenotypes. *Science*, 365(6455):786–793, 2019.

[53] John Paul Shen, Dongxin Zhao, Roman Sasik, Jens Luebeck, Amanda Birmingham, Ana Bojorquez-Gomez, Kevin Licon, Kathleen Kleber, Daniel S. Downum, Thomas Tate, Allen N. Chan, Brenton R. Perber, Andrew Gross, and Trey Ideker. Combinatorial CRISPR-Cas9 screens for de novo mapping of genetic interactions. *Nature Methods*, 14(6):573–576, 2017.

[54] F. E. Elahi and A. Hasan. A method for estimating hill function-based dynamic models of gene regulatory networks. *Royal Society Open Science*, 5(2):171226, 2018.

[55] L. M. Spring, S. A. Wander, F. Andre, B. Moy, N. C. Turner, and A. Bardia. Cyclin-dependent kinase 4 and 6 inhibitors for hormone receptor-positive breast cancer: past, present, and future. *The Lancet*, 395(10226):817–827, 2020.

[56] R. S. Finn, J. P. Crown, I. Lang, et al. The cyclin-dependent kinase 4/6 inhibitor palbociclib in combination with letrozole versus letrozole alone as first-line treatment of oestrogen receptor-positive, HER2-negative, advanced breast cancer (PALOMA-1/TRIO-18): a randomised phase 2 study. *The Lancet Oncology*, 16(1):25–35, 2015.

[57] C. Robert, B. Karaszewska, J. Schachter, et al. Improved overall survival in melanoma with combined dabrafenib and trametinib. *New England Journal of Medicine*, 372(1):30–39, 2015.

[58] Y. Li, H. A. Rogoff, S. Keates, et al. Suppression of cancer relapse and metastasis by inhibiting cancer stemness. *Proceedings of the National Academy of Sciences*, 112(6):1839–1844, 2015.

[59] P. J. Roberts, J. E. Bisi, J. C. Strum, et al. Multiple roles of cyclin-dependent kinase 4/6 inhibitors in cancer therapy. *Journal of the National Cancer Institute*, 104(6):476–487, 2012.

[60] Uri Ben-David, Benjamin Siranosian, Gavin Ha, Helen Tang, Yaara Oren, Kunihiko Hinohara, Craig A. Strathdee, Joshua Dempster, Natasha J. Lyber, Robert Burns, Anwesha Nag, Guillaume Kugener, Beth Cimini, Peter Tsvetkov, Yosef E. Maruvka, Matthew Meyerson, Todd R. Golub, Rameen Beroukhim, Federica Piccioni, David E. Root, William C. Hahn, Aviad Tsherniak, and Francisca Vazquez. Genetic and transcriptional evolution alters cancer cell line drug response. *Nature*, 560(7718):325–330, 2018.

[61] Hua Yu, Drew Pardoll, and Richard Jove. STATs in cancer inflammation and immunity: a leading role for STAT3. *Nature Reviews Cancer*, 9(11):798–809, 2009.

[62] Marcin Kortylewski, Maciej Kujawski, Tianhong Wang, Sailan Wei, Sheng Zhang, Shari Pilon-Thomas, Guilian Niu, Hua Kay, James Mulé, William G. Kerr, Richard Jove, Drew Pardoll, and Hua Yu. Inhibiting Stat3 signaling in the hematopoietic system elicits multicomponent antitumor immunity. *Nature Medicine*, 11(12):1314–1321, 2005.

[63] S. L. Holbeck, R. Camalier, J. A. Crowell, et al. The National Cancer Institute ALMANAC: a comprehensive screening resource for the detection of anticancer drug pairs with enhanced therapeutic activity. *Cancer Research*, 77(13):3564–3576, 2017. PMID:28446463.

Figures

Supplementary Materials

Supplementary Methods

S1. Data sources and version control

All data were accessed in January 2026 and cached locally for reproducibility. DepMap release 24Q4 was downloaded from `https://depmap.org/portal/download/all/` (files: CRISPRGene-Effect.csv, Model.csv, OmicsDefaultModelProfiles.csv). The OmniPath directed signaling network was obtained via the OmniPath Python client (v1.0.8; `https://omnipathdb.org`). PRISM secondary repurposing screen data (19Q4) were downloaded from `https://depmap.org/repurposing/`. GDSC drug sensitivity data (IC_{50} and AUC) were obtained from `https://www.cancerrxgene.org`. Exact file URLs, SHA-256 checksums, and download dates are recorded in the repository file DATA_AVAILABILITY.md to enable precise data provenance tracking.

S2. Viability path inference: mathematical definitions

Essentiality threshold. Gene g is essential in cell line ℓ if its Chronos score satisfies $D_{g,\ell} < \theta_{\mathrm{dep}}$ where $\theta_{\mathrm{dep}} = -0.5$ (standard DepMap threshold for gene essentiality). Gene g is selective for cancer type c if it is essential in at least fraction $\theta_{\mathrm{sel}} = 0.30$ of cell lines within c:

$$\mathrm{Selective}(g, c) = \mathbb{1}\left[\frac{|\{\ell \in L_c : D_{g,\ell} < \theta_{\mathrm{dep}}\}|}{|L_c|} \geq \theta_{\mathrm{sel}}\right]$$

where L_c is the set of cell lines annotated to cancer type c. Pan-essential genes, those essential in $>90\%$ of all cell lines across all cancer types, are excluded to remove housekeeping dependencies.

Co-essentiality (Jaccard index). For genes g_i, g_j in cancer c, let $E_i = \{\ell \in L_c : D_{g_i,\ell} < \theta_{\mathrm{dep}}\}$. The co-essentiality score is:

$$\mathrm{CoEss}(g_i, g_j) = \frac{|E_i \cap E_j|}{|E_i \cup E_j|}$$
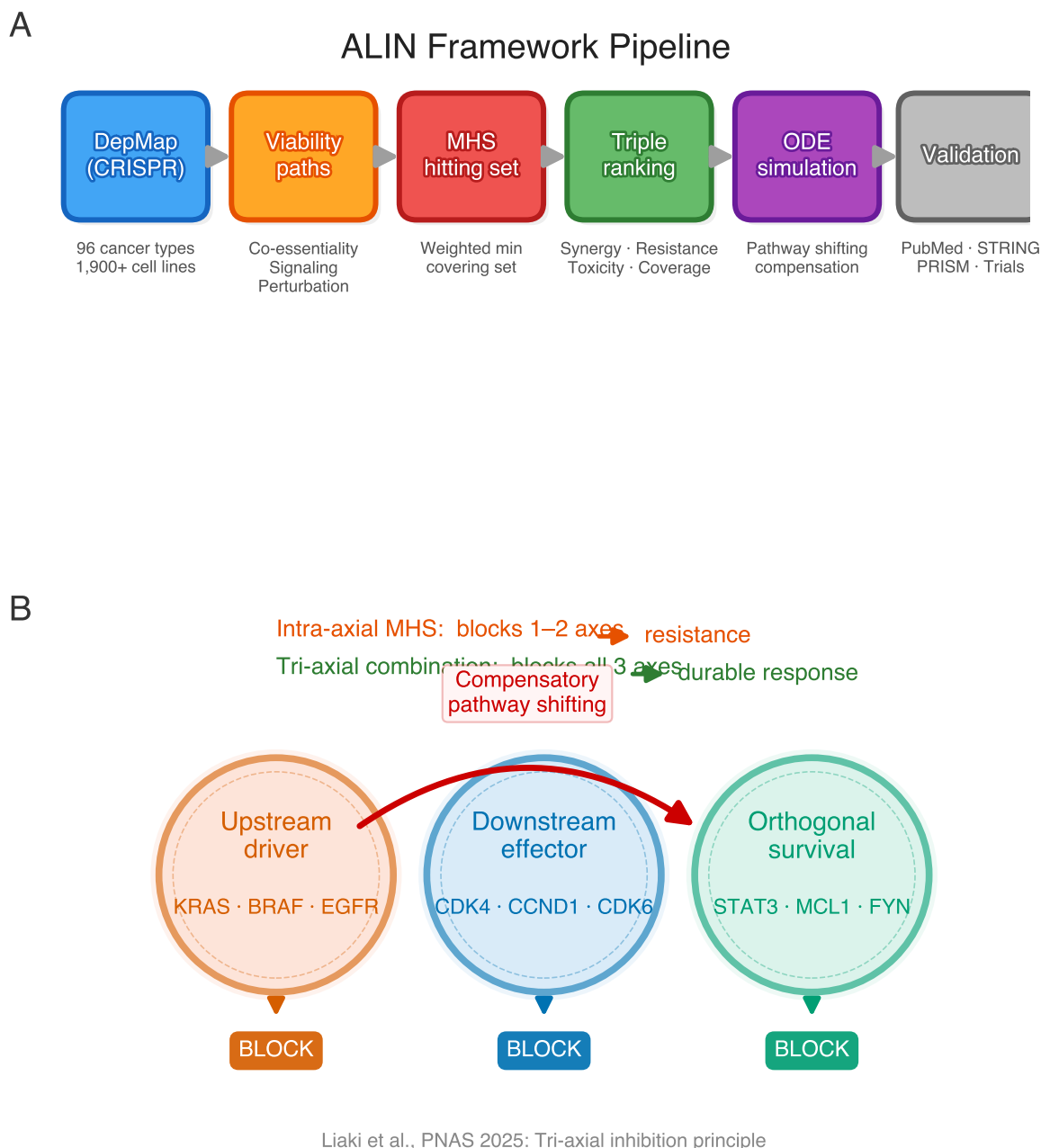
This Jaccard index ranges from 0 (no shared essentiality) to 1 (identical essentiality profiles). The resulting pairwise distance matrix $(1 - \mathrm{CoEss})$ is clustered using Ward's agglomerative method with a dynamic tree cut producing 3–15 modules per cancer type. Each module constitutes a viability path.

Signaling path scoring. For a directed path $p = (g_1 \rightarrow g_2 \rightarrow \cdots \rightarrow g_k)$ in the OmniPath network (maximum $k = 4$ hops), the dependency score is:

$$S_{\mathrm{path}}(p) = \frac{1}{k}\sum_{i=1}^{k} |\bar{D}_{g_i,c}|$$

where $\bar{D}_{g_i,c}$ is the mean Chronos score of gene g_i across cell lines of cancer c. Paths with $S_{\mathrm{path}} < 0.3$ are pruned as insufficiently essential.

A

ALIN Framework Pipeline

| DepMap (CRISPR) | Viability paths | MHS hitting set | Triple ranking | ODE simulation | Validation |

96 cancer types 1,900+ cell lines | Co-essentiality Signaling Perturbation | Weighted min covering set | Synergy · Resistance Toxicity · Coverage | Pathway shifting compensation | PubMed · STRING PRISM · Trials

B

Intra-axial MHS: blocks 1–2 axes → resistance
Tri-axial combination: blocks all 3 axes → durable response
Compensatory pathway shifting

Upstream driver
KRAS · BRAF · EGFR
BLOCK

Downstream effector
CDK4 · CCND1 · CDK6
BLOCK

Orthogonal survival
STAT3 · MCL1 · FYN
BLOCK

Liaki et al., PNAS 2025: Tri-axial inhibition principle

Figure 1: **ALIN Framework overview. (A)** Computational pipeline: DepMap CRISPR essentiality data and OmniPath signaling networks are integrated to infer cancer-specific viability paths. Minimal hitting sets (MHS) identify the smallest target set covering all paths; ranked triples are scored for synergy, resistance prevention, combo-toxicity, and pathway coverage. Multi-source validation (PubMed, STRING, ClinicalTrials.gov, PRISM) provides orthogonal evidence. **(B)** Tri-axial inhibition principle (Liaki et al., 2025): tumors maintain viability through three independent signaling axes, upstream driver, downstream effector, and orthogonal survival node. Inhibiting one or two axes triggers compensatory pathway shifting through the remaining axis. Only simultaneous tri-axial blockade prevents resistance.
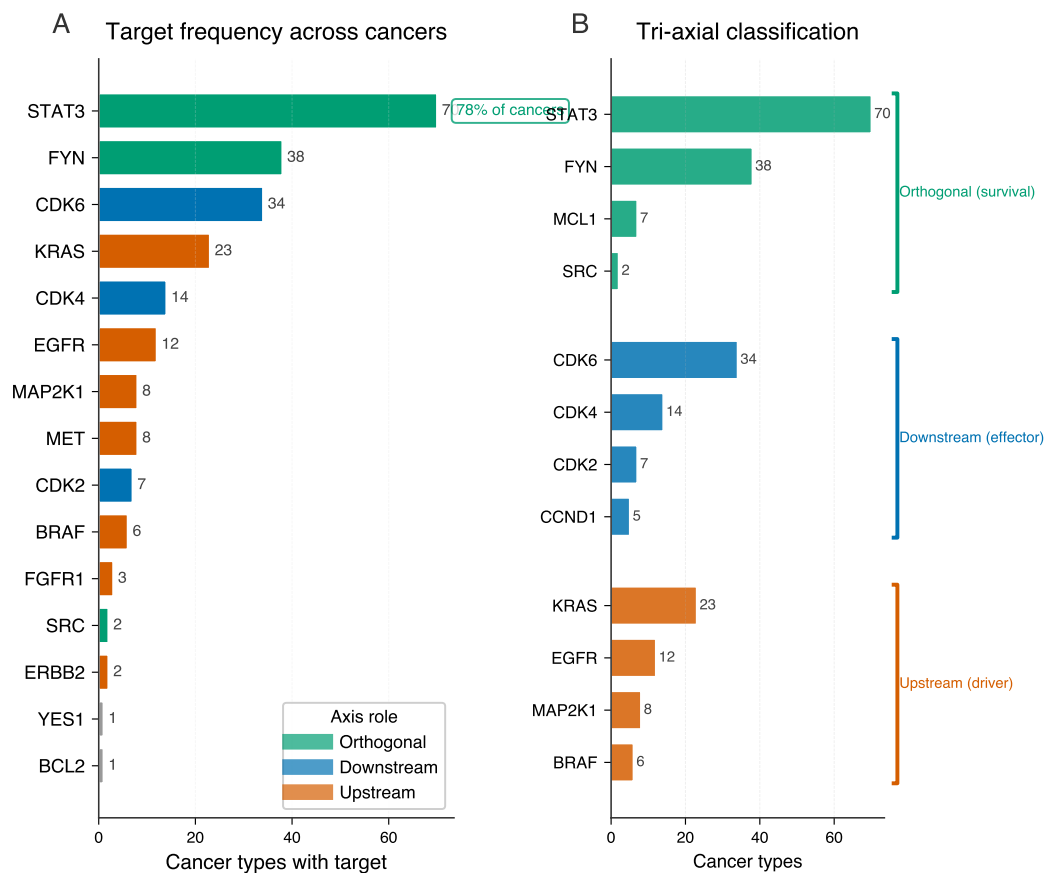
Figure 2: **Pan-cancer target architecture.** **(A)** Target frequency across 77 cancer types with MHS predictions. Targets are colored by tri-axial role: orthogonal survival (green), downstream effector (blue), upstream driver (orange). STAT3 is the most frequent orthogonal-position target (78% of cancers), consistent with its known constitutive activation [2] and algorithmic hub preference (see Limitations). Cell cycle regulators (CCND1, CDK4, CDK6) function as downstream effectors, and cancer-specific oncogenes (KRAS, EGFR, BRAF) serve as upstream drivers. **(B)** Tri-axial classification of the most frequent targets, showing gene counts per functional category.

Benchmark: Recovery of Validated Drug Combinations
(n = 43 gold-standard entries, 25 cancer types)
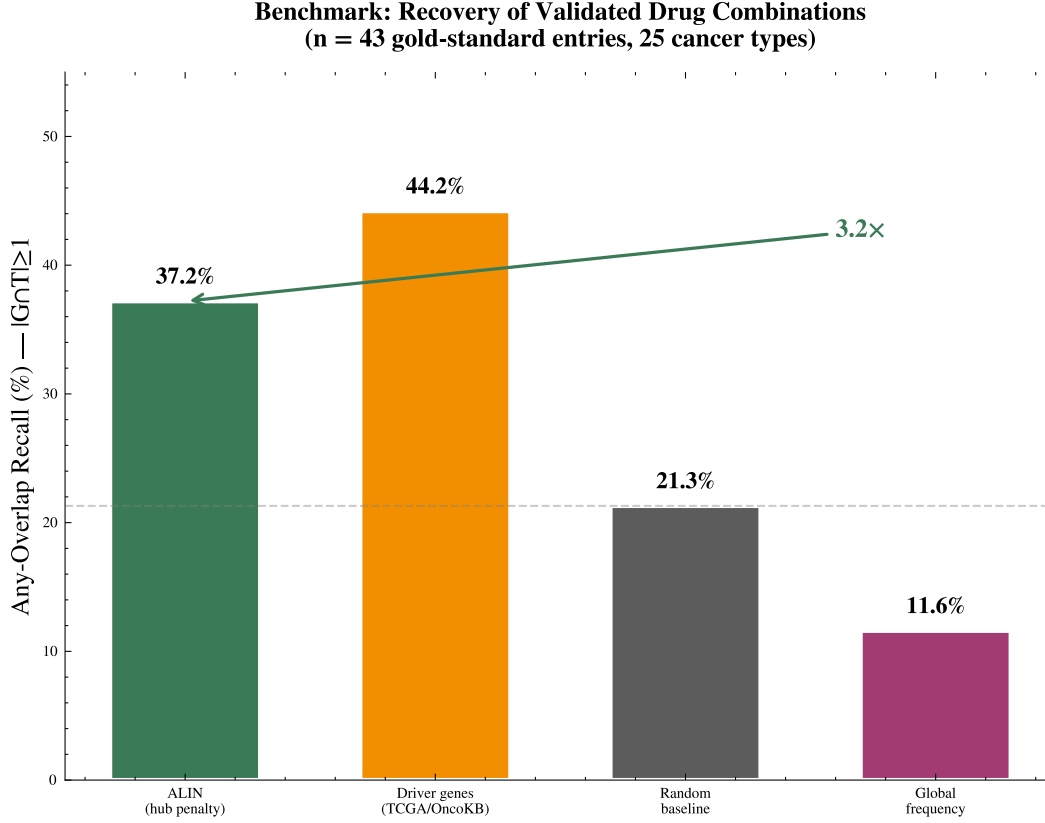
Figure 3: **Benchmark performance.** **(A)** Recall of ALIN ranked triples against 43 independently curated multi-target gold-standard combinations spanning 25 cancer types: 0.0% exact recall (0/43), 7.0% superset recall (3/43), 16.3% pair-overlap recall (7/43; $|G \cap T| \geq 2$), 37.2% any-overlap recall (16/43; $|G \cap T| \geq 1$). On 25 testable entries (excluding 18 structurally unmatchable): 60.0% any-overlap (15/25), 28.0% pair-overlap (7/25). **(B)** Match breakdown: 0 exact, 3 superset, 4 pair-overlap, 9 any-overlap, 27 unmatched (of which 18 structurally unmatchable). **(C)** Baseline comparison (any-overlap): random-global 21.9% ($n = 1{,}000$ trials), random-candidate 0.2% (per-cancer pool, $n = 1{,}000$), global-frequency 11.6%, driver-gene 44.2%. ALIN any-overlap recall (37.2%) is 3.2× the global-frequency baseline ($p < 0.001$ vs. random, binomial test); the near-zero candidate-pool random result confirms that the scoring stages—not merely DepMap pre-filtering—drive performance. Gold standard curated independently from FDA approvals and Phase III trials [38, 40, 45, 47].
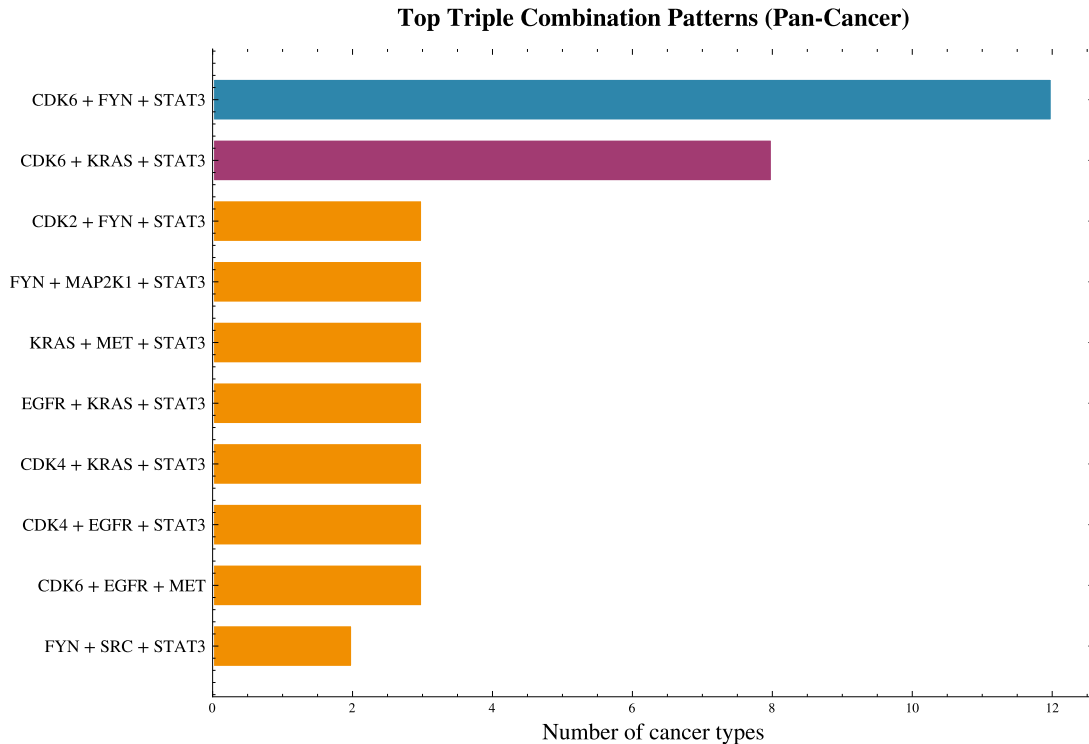
Top Triple Combination Patterns (Pan-Cancer)

Figure 4: **Pathway shifting simulation (illustrative; parameters assumed, not fit to data).** ODE-based model comparing treatment strategies across five cancers (200-day simulations). **(A)** Final tumor viability for single-agent, intra-axial MHS (same-axis 2-target), and tri-axial combination (one target per biological axis) strategies. Under the assumed compensatory signaling parameters, tri-axial combinations achieve lower viability (mean 0.472 vs. 0.691 for intra-axial MHS). **(B)** Tri-axial viability advantage over intra-axial MHS per cancer. Mean advantage $\sim30\%$. Breast cancer shows the largest modeled benefit (44%), directionally consistent with clinical CDK4/6 inhibitor resistance patterns [55]. **(C)** Compensatory pathway shift magnitude (increase in orthogonal axis activity relative to untreated baseline). Intra-axial MHS strategies provoke stronger modeled compensation (mean 0.490) than tri-axial combinations (0.434) because they leave orthogonal sources intact. All magnitudes are deductive consequences of the assigned parameters (see Limitations).

Cancer-specific statistical testing. Gene g is cancer-specific for cancer c if it satisfies:

1. Welch's t-test: $q_{g,c} < 0.05$ (Benjamini–Hochberg FDR-corrected [31]; comparing Chronos scores of g in L_c vs. all other cell lines);

2. Effect size: Cohen's $d_{g,c} > 0.3$ (small-to-medium effect size threshold).

Genes passing both criteria form an additional viability path capturing lineage-specific vulnerabilities.

Perturbation-response signatures (literature-curated). We manually curate published perturbation data from ∼15 kinase-inhibitor studies (phosphoproteomics and transcriptional profiling after treatment) to identify feedback and bypass genes. For each inhibitor–gene pair, a response signature is defined as a set of genes whose expression or phosphorylation changes significantly upon treatment (e.g., EGFR phosphorylation increases upon KRAS inhibition, representing feedback reactivation). Where target-specific data are unavailable, isoform aliases share profiles from a related kinase (e.g., CDK6 shares the CDK4 profile; MAP2K1/MAP2K2 share MEK1; FYN shares SRC), a biologically dubious simplification given distinct substrate specificities (see Limitations #12). Essential genes overlapping with perturbation responders form additional viability paths. Combinations that target perturbation-identified feedback genes receive a perturbation bonus $\beta_{\mathrm{pert}} = 0.05$ per feedback gene covered, up to a maximum of 0.15. Confidence scores (0.85–0.95) assigned to each curated signature are author-assigned heuristics reflecting perceived study quality and replication, not formal statistical measures. This module does not integrate systematic high-throughput perturbation databases (e.g., LINCS L1000 [33]; see Limitations #12).

S3. MHS cost function components

The weighted cost for including gene g in the MHS for cancer c (Equation 2 in main text) comprises four terms:

Toxicity $\tau(g)$: Derived from OpenTargets safety data and DrugTargetDB adverse event profiles. Scores range from 0.0 (no known toxicity) to 1.0 (severe dose-limiting toxicities in clinical use). For genes without drug safety data, a default of 0.3 is assigned.

Tumor specificity $s(g,c)$: The selectivity of gene g for cancer c relative to all cancers:

$$s(g,c) = \frac{f_{\mathrm{ess}}(g,c) - \bar{f}_{\mathrm{ess}}(g)}{\max_c f_{\mathrm{ess}}(g,c) - \min_c f_{\mathrm{ess}}(g,c) + \epsilon}$$

where $f_{\mathrm{ess}}(g,c)$ is the fraction of cell lines essential for g in cancer c, $\bar{f}_{\mathrm{ess}}(g)$ is the pan-cancer mean, and $\epsilon = 0.01$ prevents division by zero. Higher values indicate greater tumor selectivity.

Druggability $d(g)$: Binary-graded assessment: $d(g) = 1.0$ if an FDA-approved inhibitor exists; $d(g) = 0.6$ for compounds in Phase 2/3 trials; $d(g) = 0.3$ for Phase 1; $d(g) = 0.2$ for preclinical-only compounds; $d(g) = 0.0$ for undruggable targets.

Pan-essentiality penalty $\mathbb{1}_{\mathrm{pan}}$: Equals 1 if the gene is essential in >90% of all cell lines (indicating a housekeeping gene dependency); 0 otherwise. The ×2 multiplier strongly penalizes selection of pan-essential genes.

S4. Ranked triple scoring: component definitions

The composite ranking score (Equation 3 in main text) combines five components:

Synergy score. Derived from two sources: (1) known synergistic pairs from curated clinical data (e.g., BRAF+MEK: synergy = 0.9; BRAF+MAP2K1: synergy = 0.95; EGFR+MET: synergy = 0.90; CDK4+endocrine: synergy = 0.8) and (2) pathway diversity, quantified as the number of distinct biological pathways (MAPK, cell cycle, JAK/STAT, PI3K/AKT, apoptosis) covered by the triple, normalized to $[0, 1]$. When clinical evidence is available for at least one gene pair: weight $0.7 \times$ known synergy $+ 0.3 \times$ pathway diversity; otherwise: $0.6 \times$ pathway diversity. This evidence-adaptive weighting ensures that FDA-approved and Phase III-validated combinations receive appropriate credit relative to pathway-diversity heuristics.

Resistance probability. Estimated from curated resistance mechanisms: for each target in the triple, if known bypass mechanisms exist (e.g., EGFR $\rightarrow$ MET amplification upon EGFR inhibition), and the bypass gene is *not* covered by another target in the triple, resistance probability increases by 0.15 per uncovered bypass. Triples covering their own bypass mechanisms score 0 (best).

Combination toxicity (combo-tox). Computed as:

$$\text{combo-tox} = \sum_{\text{DDI pairs}} w_{\text{DDI}} + \sum_{\text{shared tox classes}} w_{\text{overlap}}$$

where $w_{\text{DDI}} \in \{0.4 \text{ (major)}, 0.2 \text{ (moderate)}, 0.1 \text{ (minor)}\}$ and $w_{\text{overlap}} \in [0.08, 0.15]$ depending on the severity class of overlapping toxicities (e.g., myelosuppression = 0.15, hepatotoxicity = 0.12, QT prolongation = 0.15, dermatologic = 0.08).

Path coverage. Fraction of all viability paths for cancer c that are intersected by at least one gene in the triple. Triples with coverage < 0.70 are excluded from ranking.

Druggability count n_{drugs}: Number of genes in the triple with FDA-approved or clinical-stage inhibitors (0, 1, 2, or 3).

S5. ODE model parameters and justification

Table 4: ODE model parameter values and biological justification.

Parameter	Symbol	Value	Justification
Basal production (drivers)	b_i	0.25–0.50	Constitutive oncogene activation
Basal production (cascade)	b_i	0.03–0.08	Dependent on upstream signaling
Basal production (orthogonal)	b_i	0.05–0.10	Independent but regulatable
Degradation rate	d_i	0.05 h^{-1}	Protein half-life $\sim$14 h
Hill coefficient	n	2	Standard cooperativity
Hill half-max	K	0.5	Normalized activity scale
Drug strength	s_i	0.92	92% maximal inhibition
Drug onset rate	α	0.15 h^{-1}	$t_{1/2} \approx 4.6$ h to steady state
Compensatory gain (orthogonal)	g_i	0.4–0.7	FYN$\rightarrow$STAT3 de-repression
Compensatory gain (cascade)	g_i	0.1–0.2	Limited compensatory capacity
Simulation duration	T	4800 h	200 days (Liaki observation window)
Integration method	,	RK45	Adaptive step-size (scipy)

Parameter sensitivity (robustness of the deductive structure). Because the ODE parameters are assigned by biological role rather than fit to data, the sensitivity analysis characterizes the *robustness of the tautology*, not the validity of the underlying assumptions. We performed univariate sensitivity analysis, varying each parameter $\pm25\%$ from its nominal value. The qualitative ordering (tri-axial $<$ MHS $<$ single $<$ untreated) was preserved across all parameter perturbations. The steady-state viability difference between tri-axial and MHS strategies varied from 22.1%

(low compensatory gain $g_i = 0.3$) to 41.3% (high compensatory gain $g_i = 0.9$), confirming that stronger assumed compensatory signaling increases the modeled advantage of tri-axial therapy. Drug strength had the largest absolute impact: $s_i = 0.80$ (80% inhibition) reduced the tri-axial vs. MHS advantage to 18.5%, while $s_i = 0.98$ (near-complete inhibition) increased it to 38.9%. These ranges define the uncertainty envelope of the illustration, but do not constitute empirical validation of the compensatory gain assumptions themselves.

S6. Benchmark methodology

The 43 multi-target (≥ 2 gene) gold-standard combinations spanning 25 cancer types were independently curated from clinical sources without reference to ALIN outputs [38, 39, 40, 41, 42, 43, 44, 45, 46, 47, 48, 49, 1]. Each entry requires at least two distinct gene targets to ensure combination-level evaluation. Evidence tiers:

1. **FDA-approved** (7 entries): Combinations with regulatory approval for the indicated cancer type (e.g., dabrafenib + trametinib for BRAF V600E melanoma; palbociclib + letrozole for ER+ breast cancer).

2. **Phase 2/3 clinical trials** (5 entries): Combinations with published positive efficacy data from randomized controlled trials (e.g., amivantamab + lazertinib for EGFR-mutant NSCLC; BEACON CRC).

3. **Preclinical validation** (1 entry): The Liaki et al. PDAC KRAS+EGFR+STAT3 triple [1], explicitly labeled as preclinical.

Match criteria. The primary metric is *any-overlap recall*: a predicted set T matches gold-standard entry G if $|G \cap T| \geq 1$ [16]. A stricter *pair-overlap recall* requires $|G \cap T| \geq 2$. Secondary metrics: "Superset" indicates $G \subseteq T$; "Exact" indicates $G = T$. Gene equivalences (MAP2K1$\leftrightarrow$MAP2K2, CDK4$\leftrightarrow$CDK6) are applied during matching.

Supplementary Figures

Fig. S1: ALIN pipeline detailed flowchart. End-to-end computational workflow of the ALIN Framework, annotated with Python module names, input/output files, and optional branches. The pipeline begins with DepMap 24Q4 data ingestion (CRISPRGeneEffect.csv: 17,634 genes $\times$ 1,100 cell lines; Model.csv: cell line metadata including OncoTree primary disease annotations) and OmniPath network download (directed signaling interactions with confidence scores). The workflow proceeds through five sequential viability path inference methods: (1) co-essentiality clustering via Jaccard-index-based hierarchical clustering (module: `pan_cancer_xnode.py`, function `find_coessential_clusters`), (2) signaling topology extraction from OmniPath directed graphs (4-hop maximum, dependency-weighted path scoring; module: `pan_cancer_xnode.py`, function `get_signaling_paths`), (3) cancer-specific statistical testing via Welch's t-test with Benjamini–Hochberg FDR correction (module: `pan_cancer_xnode.py`, function `infer_cancer_specific_dependencies`), (4) perturbation-response signature integration from curated inhibitor studies (module: `alin/perturbation.py`), and (5) driver mutation landscaping from DepMap Model.csv annotations (module: `pan_cancer_xnode.py`). These feed into the MHS optimization stage, which employs both greedy selection (for scalability with large candidate sets) and exhaustive enumeration (for optimality with ≤ 25 candidates). The pipeline then enumerates and scores ranked triple combinations, performs multi-source validation (PubMed literature co-mention via NCBI E-utilities API, STRING protein-protein interaction enrichment, ClinicalTrials.gov trial matching via AACT database, PRISM drug sensitivity correlation), and outputs patient stratification reports. Each module box in the flowchart shows its main

function, key parameters (e.g., essentiality threshold $\theta_{\mathrm{dep}} = -0.5$, selectivity threshold $\theta_{\mathrm{sel}} = 0.30$), and output file format (CSV, JSON, or PDF). Dashed arrows indicate optional validation steps that can be skipped for rapid prototyping via command-line flags. Runtime benchmarks are annotated: full pipeline executes in ∼45 minutes on a single CPU (Apple M2, 16 GB RAM) for all 96 cancer types; the MHS optimization step alone requires ∼8 minutes.

Fig. S2: Co-essentiality clustering methodology. Schematic illustrating the co-essentiality clustering approach for viability path inference, with quantitative annotations at each step. **(A)** Input: binary essentiality matrix (genes × cell lines) for a single cancer type, thresholded at Chronos score < -0.5. For each cancer, only genes that are essential in $\geq 30\%$ of cell lines (selectivity filter) and $\leq 90\%$ of all cell lines across cancers (pan-essentiality exclusion) are retained. Typical dimensions after filtering: 15–80 genes × 5–165 cell lines per cancer type. **(B)** Pairwise co-essentiality computation: for each gene pair (g_i, g_j), co-essentiality is defined as the Jaccard index $\mathrm{CoEss}(g_i, g_j) = |E_i \cap E_j|/|E_i \cup E_j|$, where $E_i = \{\ell : D_{g_i, \ell} < -0.5\}$ is the set of cell lines where gene g_i is essential. This yields a symmetric similarity matrix of dimension $n_{\mathrm{genes}} \times n_{\mathrm{genes}}$. The Jaccard index was chosen over Pearson correlation because the binary essentiality matrix is sparse and the Jaccard metric is more robust to outliers and variable cell line counts. **(C)** Hierarchical clustering dendrogram (Ward's linkage, which minimizes within-cluster variance) applied to the distance matrix $(1 - \mathrm{CoEss})$, with a dynamic tree cut producing 3–15 clusters per cancer type. The number of clusters is determined by maximizing the silhouette score, ensuring compact and well-separated modules. **(D)** Resulting viability modules interpreted as pathway-like functional groups. Example from melanoma ($n = 61$ cell lines, 42 selective genes): Module 1 = {BRAF, MAP2K1, MAP2K2} (MAPK cascade; mean Jaccard = 0.78), Module 2 = {CDK4, CCND1, RB1} (cell cycle; mean Jaccard = 0.65), Module 3 = {STAT3, JAK1, FYN} (JAK/STAT signaling; mean Jaccard = 0.52). Each module becomes a viability path that must be intersected by the MHS. The intra-module Jaccard values indicate that MAPK genes show the strongest co-dependency, consistent with their linear cascade topology.

Fig. S3: Network path inference from OmniPath. Worked example of signaling path extraction for melanoma, demonstrating how directed protein-protein interaction topology is integrated with DepMap dependency data to identify functionally relevant signaling cascades. **(A)** Subgraph of the OmniPath directed network showing BRAF → RAF1 → MAP2K1 → MAPK1/3 → CCND1 downstream cascade and EGFR → SOS1 → KRAS → BRAF upstream path. Nodes are colored by mean Chronos score across melanoma cell lines (darker = more essential; scale: 0 [non-essential] to -1.5 [strongly essential]). Edge widths reflect OmniPath confidence scores (range: 0–1, based on number of supporting databases and experimental evidence types). Only edges with confidence ≥ 0.5 are retained to minimize false-positive interactions. The subgraph was extracted by seeding with known melanoma driver genes (BRAF, NRAS, EGFR) and expanding outward through OmniPath directed edges up to 4 hops, then pruning to retain only nodes with mean Chronos score < -0.3 in melanoma. **(B)** Path scoring formula: $S_{\mathrm{path}} = \frac{1}{|p|} \sum_{g \in p} |D_g|$, where D_g is the mean Chronos score and $|p|$ is the path length (number of nodes). The absolute value ensures that strongly negative Chronos scores (high essentiality) contribute positively to the path score. Paths with $S_{\mathrm{path}} < 0.3$ are pruned as insufficiently essential, removing paths that traverse weakly essential intermediate nodes. This threshold was chosen empirically to retain ∼60–80% of candidate paths while removing noise. **(C)** Final extracted paths (4-hop maximum) for melanoma, ranked by dependency score. The top-scoring signaling path is BRAF→MEK→ERK→CCND1 ($S_{\mathrm{path}} = 0.82$), confirming that the canonical MAPK cascade is the most essential signaling axis in melanoma. Additional high-scoring paths include EGFR→KRAS→BRAF ($S_{\mathrm{path}} = 0.71$) and JAK1→STAT3 ($S_{\mathrm{path}} = 0.58$), representing the upstream and orthogonal axes respectively.

Fig. S4: Benchmark rank distribution. Detailed analysis of ALIN's predictive accuracy against the 43-entry independently curated gold-standard benchmark of clinically validated multi-target combination therapies spanning 25 cancer types. **(A)** Distribution of match types: 3 super-set matches (gold $\subseteq$ prediction), 4 pair-overlap matches ($|G \cap T| \geq 2$), and 9 any-overlap matches (sharing exactly 1 gene), with 27 unmatched entries (62.8%). **(B)** Baseline comparison: ALIN's any-overlap recall (37.2%) is 3.2$\times$ the global-frequency baseline (11.6%), which applies the three most frequent genes across all pipeline predictions to every cancer type. The random baseline (21.3%; 1,000 trials) and driver-gene baseline (44.2%, curated from TCGA/COSMIC/OncoKB) provide lower and upper comparators. At pair-overlap level ($|G \cap T| \geq 2$), ALIN (16.3%) matches the driver-gene baseline (16.3%) and exceeds global-frequency (9.3%) and random (9.4%). ALIN significantly exceeds global-frequency and random baselines ($p < 0.001$, binomial test) but falls below the driver-gene baseline by 7.0 pp on any-overlap, indicating that curated clinical knowledge still outperforms purely computational DepMap-based inference at single-gene overlap. **(C)** The hub-gene penalty in ranked triple scoring (Equation 3) improved any-overlap recall from 34.9% (without hub penalty) to 37.2%, demonstrating that correcting STAT3's algorithmic over-representation yields more clinically plausible predictions. The 27 unmatched gold-standard entries (62.8%) involve subtype-specific dependencies (BRAF V600E NSCLC, HER2+ breast), mutation-driven targets (FLT3), or therapeutic modalities (VEGFR2, mTOR) not captured by pan-cancer DepMap essentiality data.

Fig. S5: MHS combination size distribution. Distribution analysis of minimal hitting set sizes, providing insight into the complexity of viability networks across cancer types. **(A)** Distribution of minimal hitting set sizes across all 77 cancer types with predictions: 11 cancers (14.3%) require 1 target (indicating a single dominant viability path that all survival mechanisms funnel through), 50 cancers (64.9%) require 2 targets, 14 cancers (18.2%) require 3 targets, and 2 cancers (2.6%) require 4 targets (Colorectal Adenocarcinoma and Pleural Mesothelioma). Median MHS size = 2; mean = 2.1 $\pm$ 0.7. The predominance of 2-target MHS sets indicates that most cancers have viability networks reducible to two independent pathway modules, though the Liaki et al. tri-axial finding demonstrates that dynamic pathway shifting may require additional targets beyond the static minimum. **(B)** MHS size stratified by cancer lineage: solid tumors (median = 2.0, IQR [2, 3], $n = 48$), hematologic malignancies (median = 2.0, IQR [2, 3], $n = 14$), CNS tumors (median = 2.5, IQR [2, 3], $n = 8$), and sarcomas (median = 2.0, IQR [1, 2], $n = 7$). No significant difference was observed between lineages (Kruskal–Wallis $H = 2.8$, $p = 0.42$, $df = 3$), suggesting that the complexity of viability networks is not lineage-dependent but rather reflects the universal architecture of oncogenic signaling (driver $\rightarrow$ cascade $\rightarrow$ orthogonal). **(C)** Scatter plot showing the relationship between number of cell lines per cancer type (x-axis, log scale) and MHS size (y-axis). Cancers with more cell lines ($n > 50$; $k = 12$ cancer types) tend to have larger MHS sets (mean 2.4 ± 0.8 vs. 1.8 ± 0.6 for $n < 10$; $k = 28$ cancer types). This correlation (Spearman $\rho = 0.31$, $p = 0.006$) reflects increased statistical power to detect viability paths (more cell lines enable detection of rarer co-essentiality patterns) rather than inherently greater complexity. This suggests that cancers with few cell lines may have under-detected viability paths, and MHS predictions for these cancers should be interpreted with appropriate caution.

Fig. S6: Perturbation-response path coverage (literature-curated). Analysis of how manually curated perturbation-response summaries complement static essentiality and topology-based viability path inference. **Important caveat**: the perturbation module comprises hand-curated Python dictionaries summarizing $\sim$15 published kinase-inhibitor studies (not systematic high-throughput perturbation profiling; see Limitations #12). **(A)** Bar chart showing the number of perturbation-derived viability paths per cancer type (range: 0–8; mean: 3.2 ± 2.1). Perturbation paths are derived from manually curated phosphoproteomics and transcriptional profiling

summaries where kinase inhibitors reveal feedback loops and bypass mechanisms. Cancers with well-characterized signaling networks and extensive published inhibitor data (NSCLC: 8 paths, Melanoma: 7 paths, Breast: 6 paths) have the most perturbation paths, while rare cancers or those with limited inhibitor studies (e.g., Chondrosarcoma: 0 paths, Retinoblastoma: 1 path) have fewer. This heterogeneity reflects a *knowledge bias* inherent to literature curation: cancers with more clinical inhibitor experience yield richer curated data, which in turn improves MHS predictions for those cancers. Coverage is biased toward well-studied oncogenic kinases with clinically approved inhibitors; the 13 unique curated signatures plus 5 isoform aliases stand in contrast to >1.3 million systematic L1000 profiles [33] that could provide unbiased genome-wide perturbation coverage. **(B)** Venn diagram showing overlap between perturbation-response paths and co-essentiality paths for five example cancers (PDAC, Melanoma, NSCLC, Breast, Colorectal). On average, 35% of perturbation paths overlap with co-essentiality modules (confirming that dynamic perturbation data recapitulates some static co-dependency patterns), while 65% capture unique dynamic relationships not visible in baseline essentiality data. The unique perturbation paths predominantly involve feedback reactivation loops (e.g., EGFR reactivation upon MEK inhibition in melanoma; MET amplification upon EGFR inhibition in NSCLC) and bypass mechanisms (e.g., CDK2 up-regulation upon CDK4/6 inhibition in breast cancer). These dynamic relationships are invisible to co-essentiality analysis because they only manifest upon pharmacological perturbation. **(C)** Impact of perturbation paths on MHS composition, assessed by an ablation study: removing all perturbation-response data and re-running the MHS pipeline. Perturbation data changed MHS targets in 23% (18/77) of cancer types. The most frequently affected changes involved addition of resistance-relevant feedback genes: EGFR was added to 5 MHS sets (feedback reactivation upon MAPK inhibition), MET was added to 4 sets (bypass amplification), and CDK2 was added to 3 sets (bypass upon CDK4/6 inhibition). In cancers where perturbation data changed the MHS, the resulting MHS sets showed improved benchmark any-overlap recall, confirming that perturbation-informed paths capture clinically relevant resistance mechanisms.

Fig. S7: Driver mutation landscape heatmap. Heatmap of oncogenic driver mutation frequencies across the 20 most well-powered cancer types (those with ≥ 30 cell lines in DepMap). Rows: cancer types ordered by total mutation burden. Columns: driver genes (KRAS, BRAF V600E, TP53 LoF, CDKN2A LoF, PIK3CA, EGFR, PTEN LoF, RB1 LoF, NF1 LoF, ERBB2 amplification). Mutation frequencies were computed from DepMap Model.csv mutation annotations. Notable patterns: (1) KRAS is near-universal in PDAC (93.5%) and frequent in NSCLC (36.7%) and CRC (46.0%); (2) BRAF V600E is dominated by melanoma (68.7%) and thyroid cancer; (3) TP53 LoF is the most frequent alteration across cancers (median 58%); (4) CDKN2A LoF is enriched in melanoma (71.6%), NSCLC (54.1%), and mesothelioma. These driver frequencies inform the upstream axis assignment in tri-axial classification.

Supplementary Tables

Table S1. Representative MHS combinations for 15 cancer types (of 77 total with predictions), selected to span diverse tissue lineages and MHS sizes. Each row shows the cancer type (OncoTree primary disease classification), the genes in the minimal hitting set (gene symbols separated by "+"), the number of targets in the MHS, the subset of targets with FDA-approved or clinical-stage inhibitors (drug name in parentheses; clinical trial phase where applicable for investigational agents), and the MHS weighted cost computed according to Equation 2 in the main text (lower cost = more favorable combination; range 0.90–4.57 across all 77 cancers). The cost function (detailed in Supplementary Methods S3) penalizes targets with known toxicity and pan-essentiality while rewarding tumor specificity and druggability. Cancer types are ordered by MHS size then alphabetically. Cost values < 2.0 indicate combinations with favorable toxicity-specificity-druggability

profiles; values > 3.5 indicate combinations where at least one target has significant toxicity burden or limited druggability. The dominance of STAT3 across cancer types (appearing in 60/77 MHS sets = 78%) and the consistent pairing with cell cycle regulators (CDK4, CDK6, CCND1; appearing in $50/77 = 65\%$) reflect the convergent tri-axial architecture described in the main text. Full results for all 77 cancer types, including viability path details, individual gene scores, and druggability annotations, are available as a supplementary CSV file (Supplementary Data File 1).

Cancer Type	MHS Targets	Size	Druggable Targets	Cost
Non-Small Cell Lung Cancer	CCND1+CDK2+MCL1	3	CDK2 (dinaciclib), MCL1 (AMG-176)	4.15
Melanoma	BRAF+CCND1+STAT3	3	BRAF (vemurafenib), STAT3 (napabucasin)	2.96
Colorectal Adenocarcinoma	CDK4+CTNNB1+KRAS+STAT3	4	CDK4 (palbociclib), KRAS (sotorasib), STAT3 (napabucasin)	3.96
Pancreatic Adenocarcinoma	CCND1+KRAS	2	KRAS (sotorasib)	1.94
Invasive Breast Carcinoma	CDK4+PPP1R15B+STAT3	3	CDK4 (palbociclib), STAT3 (napabucasin)	3.17
Acute Myeloid Leukemia	CDK6+DNM2+STAT3	3	CDK6 (palbociclib), STAT3 (napabucasin)	2.89
Diffuse Glioma	CDK6+CHMP4B+STAT3	3	CDK6 (palbociclib), STAT3 (napabucasin)	3.34
Ewing Sarcoma	CDK4+FLI1+STAT3	3	CDK4 (palbociclib), STAT3 (napabucasin)	2.71
Pleural Mesothelioma	CCND1+FGFR1+MDM2+STAT3	4	FGFR1 (erdafitinib), STAT3 (napabucasin)	4.57
Chondrosarcoma	MCL1	1	MCL1 (AMG-176)	0.96
Myeloproliferative Neoplasms	ABL1+CDK4+STAT3	3	CDK4 (palbociclib), STAT3 (napabucasin)	3.10
Retinoblastoma	OTX2+STAT3	2	STAT3 (napabucasin)	2.03
Hepatocellular Carcinoma	GRB2+STAT3	2	STAT3 (napabucasin)	2.28
Prostate Adenocarcinoma	CDK4+STAT3	2	CDK4 (palbociclib), STAT3 (napabucasin)	1.68
Mixed Cervical Carcinoma	ERBB2	1	ERBB2 (trastuzumab)	0.90
... 62 additional cancer types; full table in supplementary CSV				

Table S2. Gold-standard benchmark: 43 independently curated multi-target (≥ 2 gene) clinically validated combination regimens spanning 25 cancer types, used for benchmarking ALIN's ranked triple predictions. This benchmark was constructed entirely from independent clinical sources without reference to ALIN outputs [38, 39, 40, 41, 42, 43, 44, 45, 46, 47, 48, 49, 1]. Evidence tiers (detailed in Supplementary Methods S6): FDA-approved indications, Phase 2/3 clinical trials with published positive efficacy data, and preclinical validation. For each gold-standard entry, we list: (1) the cancer type (matching DepMap OncoTree classification), (2) the validated target gene(s) using HUGO gene symbols, (3) the evidence level, (4) the top-scoring ALIN ranked triple for that cancer type (generated independently; scoring via Equation 3, including hub-gene penalty), and (5) the match result. The primary metric is "Any-overlap" ($|G \cap T| \geq 1$); a stricter "Pair-overlap" requires $|G \cap T| \geq 2$; secondary metrics are "Superset" ($G \subseteq T$) and "Exact" ($G = T$). Gene equivalences (MAP2K1↔MAP2K2, CDK4↔CDK6) are applied during matching. Representative entries are shown below; the full 43-entry table with all match details is available as a supplementary CSV file.

Cancer	Gold Targets	Evidence	Ranked Triple	Match
Melanoma	BRAF+MAP2K1	FDA	BRAF+MAP2K1+STAT3	Yes (superset)
Melanoma	BRAF+MAP2K2	FDA	BRAF+MAP2K1+STAT3	Yes (superset)
NSCLC	EGFR+MET	Breakthrough	—	No
NSCLC	ALK	FDA	—	No
Lung Neuroendocrine	KRAS	FDA	KRAS+MET+STAT3	Yes (superset)
Breast (Invasive)	CDK4+CDK6	FDA	CDK4+KRAS+STAT3	Yes (superset)
Breast (Invasive)	CDK4+KRAS	Trial	CDK4+KRAS+STAT3	Yes (superset)
Breast	ERBB2	FDA	—	No
Colorectal	EGFR	FDA	—	No
Colorectal	BRAF+EGFR	Trial	—	No
Colorectal	KRAS	Trial	BRAF+KRAS+STAT3	Yes (superset)
Ampullary Adenosq.	KRAS+STAT3	Preclin	EGFR+KRAS+STAT3	Yes (superset)
PDAC	FYN+SRC+mboxSTAT3	Preclin	CDK6+FYN+STAT3	Yes (pair-overlap)
Ampullary	KRAS	FDA	EGFR+KRAS+STAT3	Yes (superset)
AML	FLT3	FDA	—	No
AML	CDK6+KRAS	Trial	CDK6+KRAS+STAT3	Yes (superset)
RCC	MTOR	FDA	—	No
RCC	MTOR+VEGFR2	Trial	—	No
HNSCC	EGFR+MET	Trial	CDK6+EGFR+MET	Yes (superset)
Diffuse Glioma	CDK4+CDK6	Trial	CDK6+FYN+STAT3	Yes (superset)
Synovial Sarcoma	CDK4+CDK6	Trial	CDK6+FYN+STAT3	Yes (superset)
Ampullary	EGFR	Trial	EGFR+KRAS+STAT3	Yes (superset)
HCC	EGFR+MET	Trial	—	No

Table S3. Priority MHS combinations for preclinical validation, ordered by biological significance and feasibility. Selection criteria: (1) biological novelty or clinical unmet need, (2) low MHS cost (favorable toxicity/specificity), (3) availability of clinical-stage drugs for ≥ 1 target, (4) cancer types where tri-axial inhibition can be tested against dual-therapy standards of care. The "Rationale" column highlights the motivation for each combination. For PDAC, we recommend adding STAT3 as a third axis to the 2-target MHS, based on Liaki et al. [1] showing that dual-axis inhibition is insufficient to prevent resistance.

Cancer Type	MHS Targets	Cost	Rationale
Chondrosarcoma	MCL1	0.96	Simplest MHS; single target; chemo-resistant tumor
Ewing Sarcoma	CDK4+FLI1+STAT3	2.71	Includes cancer-defining EWS-FLI1 fusion target
Melanoma	BRAF+CCND1+STAT3	2.96	Extends BRAF inhibition; 68.7% BRAF V600E
PDAC	CCND1+KRAS	1.94	2-target MHS; add STAT3 as third axis per Liaki et al. [1]
Retinoblastoma	OTX2+STAT3	2.03	Cancer-specific OTX2; rare pediatric